

Prussian Blue Analogues for Sodium-Ion Battery Cathodes: A Review of Mechanistic Insights, Current Challenges, and Future Pathways

Yang Xiao, Jun Xiao, Hangkai Zhao, Jiayi Li, Guilai Zhang, Dingyi Zhang, Xin Guo, Hong Gao,* Yong Wang, Jun Chen,* Guoxiu Wang, and Hao Liu*

Prussian blue analogues (PBAs) have emerged as highly promising cathode materials for sodium-ion batteries (SIBs) due to their affordability, facile synthesis, porous framework, and high theoretical capacity. Despite their considerable potential, practical applications of PBAs face significant challenges that limit their performance. This review offers a comprehensive retrospective analysis of PBAs' development history as cathode materials, delving into their reaction mechanisms, including charge compensation and ion diffusion mechanisms. Furthermore, to overcome these challenges, a range of improvement strategies are proposed, encompassing modifications in synthesis techniques and enhancements in structural stability. Finally, the commercial viability of PBAs is examined, alongside discussions on advanced synthesis methods and existing concerns regarding cost and safety, aiming to foster ongoing advancements of PBAs for practical SIBs.

sodium resources, SIBs also feature a “rocking chair” mechanism akin to LIBs. The critical progression of SIBs relies on the development of suitable cathode materials, which stand as a pivotal factor driving their advancement. Ideal cathode materials for SIBs are expected to possess high redox potential, substantial mass and volumetric capacities, excellent structural stability, and high electronic and ionic conductivity.^[3] These characteristics collectively enhance energy density, extend cycling life, and ensure the efficient functioning of SIBs. The development of safe, non-toxic, cost-effective, and easily preparable cathode materials is integral to reducing the overall cost of SIBs, thus solidifying their position as a viable alternative in the evolving landscape of energy storage technologies.

1. Introduction

The rapid advancements in electric vehicles and smart grid energy storage systems have solidified secondary batteries as the pinnacle of efficient energy storage technology, characterized by swift response and high energy density. Despite the advantages, the widespread application of lithium-ion batteries (LIBs) faces a substantial hurdle due to the limited availability of lithium resources.^[1,2] In response to this challenge, the strategic significance of SIBs has come to the forefront. Boasting abundant


Researchers have conducted substantial advancements in the exploration of cathode materials, focusing on transition metal layer oxides (TMOs), polyanionic compounds, organic materials, and PBAs.^[4] PBAs gained attention in SIBs, notably through Cui et al.'s work in 2011,^[5] which highlighted $K_{0.71}Cu[Fe(CN)_{6}]_{0.72}$ cathode for its low internal lattice stress and structural stability. Serving as exemplary sustainable cathode materials for SIBs, PBAs offer distinct advantages: (1) A robust framework with three-dimensional diffusion channels, ensuring efficient alkali metal transport and excellent cyclic stability; (2) Their

Y. Xiao, H. Zhao, J. Li, G. Zhang, D. Zhang, H. Gao, Y. Wang
Joint International Laboratory on Environmental and Energy Frontier
Materials
School of Environmental and Chemical Engineering
Shanghai University
Shanghai 200444, China
E-mail: hgao1122@shu.edu.cn

J. Xiao, X. Guo
Faculty of Materials Science and Energy Engineering/
Institute of Technology for Carbon Neutrality
Shenzhen Institute of Advanced Technology
Chinese Academy of Sciences
Shenzhen, Guangdong 518055, China

J. Chen
Intelligent Polymer Research Institute
Innovation Campus
University of Wollongong
Squires Way, North Wollongong, NSW 2500, Australia
E-mail: junc@uow.edu.au

G. Wang, H. Liu
Centre for Clean Energy Technology
University of Technology Sydney
Broadway, Sydney, NSW 2007, Australia
E-mail: hao.liu@uts.edu.au

 The ORCID identification number(s) for the author(s) of this article can be found under <https://doi.org/10.1002/smll.202401957>

© 2024 The Authors. Small published by Wiley-VCH GmbH. This is an open access article under the terms of the [Creative Commons Attribution-NonCommercial](https://creativecommons.org/licenses/by-nc/4.0/) License, which permits use, distribution and reproduction in any medium, provided the original work is properly cited and is not used for commercial purposes.

DOI: 10.1002/smll.202401957

cost-effectiveness, abundance of raw materials, and straightforward synthesis methods make PBAs well-suited for large-scale energy storage applications, contributing to the economic feasibility of SIBs; (3) The presence of abundant redox couples and highly reversible phase transitions further enhance their efficiency in charge storage.^[1,3,6] The chemical formula, $\text{Na}_x\text{M}[\text{Fe}(\text{CN})_6]$, underscores the versatility of PBAs, accommodating various transition metals like Fe, Mn, Ni, Co, or Cu, for tailored applications in SIBs. The lattice structure of PBAs comprises $[\text{Fe}(\text{CN})_6]^{4-}$ units and transition metal M, forming a 3D framework. In this structure, the transition metal M is positioned at the vertices of a face-centered cube, and $-\text{C}\equiv\text{N}-$ are located along the edges of the cube. Sodium ions occupy the interstitial positions within the cube. Unlike TMOs and polyanionic compounds, PBAs exhibit significant sodium storage interstitial sites and wide channels in the $\langle 100 \rangle$ direction.^[7] Additionally, PBAs feature two distinct redox-active centers: $\text{M}^{2+/3+}$ and $\text{Fe}^{2+/3+}$, allowing comprehensive electrochemical redox reactions (where M can be Fe, Co, Mn, etc.). Consequently, PBAs demonstrate a theoretical specific capacity of approximately 170 mAh g^{-1} , surpassing the capacities of most TMOs ($100\text{--}150 \text{ mAh g}^{-1}$)^[8–11] and polyanionic compounds ($\approx 120 \text{ mAh g}^{-1}$).^[12] Despite their promising properties, PBAs face several challenges in their application. These include lattice vacancies and lattice water, which arise from the co-precipitation reaction and non-uniform nucleation rates, ultimately leading to low sodium storage content. Activating most low-spin states of Fe poses difficulty. Additionally, irreversible phase transitions and lattice distortions occur during electrochemical cycling, along with Jahn-Teller effects in Mn-based PBAs, all of which can contribute to structural collapse, significantly impacting the electrochemical performance of PBAs. Parasite reactions occurring at the interface with the electrolyte, as well as stress during Na^+ insertion/desertion processes that are not promptly alleviated, can also bring about collapse of the structural crystal.

This review offers a comprehensive exploration of the pivotal role played by PBAs in SIBs. It meticulously traces the developmental trajectory of PBAs and identifies the challenges they encounter, presenting a diverse array of solutions. These solutions encompass synthesis modifications and optimizations of crystal structures, including techniques such as heat treatment, vacancy repair, surface coating, and element substitution. Additionally, the review scrutinizes critical aspects such as the evolution of crystal structures across cubic, monoclinic, rhombohedral, and tetragonal phases. It provides insights into the charge compensation mechanisms of 3d transition metal ions and elucidates single/cooperative ion diffusion mechanisms. Furthermore, the review explores cutting-edge synthesis techniques tailored to enhance performance. Comprehensive evaluations of factors such as cost, safety considerations, and commercial prospects are undertaken. Through this rigorous analysis, the review aims to furnish invaluable insights that propel the advancement and practical implementation of PBAs in SIB technology.

2. Historical Development of Prussian Blue Analogues in SIBs

The development history of PBAs spans centuries, originating from their discovery in Berlin in 1706 as metal-organic framing

materials primarily used in dyes for oil paintings and textiles.^[13] In recent years, Prussian Blue (PB) and PBAs have found expanded applications, including catalysis,^[14] biosensing,^[15] electrochemical chromic devices, optically controlled films,^[16] and even nanoparticles for tumor intervention,^[17] showcasing a promising developmental trajectory. Notably, PB and PBAs have garnered significant attention as electrode materials, particularly in their role as cathodes for SIBs, as shown in **Figure 1**.

In 2015, Goodenough's group introduced an air-stable $\text{R-Na}_{1.92}\text{Fe}[\text{Fe}(\text{CN})_6]$ material with a rhombohedral structure, demonstrating its viability as a scalable,^[18] cost-effective cathode for SIBs with exceptional capacity, cycling stability, and rate performance. Subsequent studies elucidated the iron redox mechanism via synchrotron-based soft X-ray absorption spectroscopy, revealing crucial correlations between physical properties and cell performance. Further advancements, such as the successful fabrication of dehydrated iron hexacyanoferrate with high Na^+ concentration, enabled the fabrication of SIBs with non-sodium metal anodes.

In-depth investigations highlighted the critical role of nucleation rate in PBA synthesis, with rapid precipitation leading to detrimental vacancies and interstitial water formation within the crystal structure, resulting in poor electrochemical performance. Strategies to mitigate these issues emerged, Wu et al.^[19] used sodium citrate to regulate coordination rates between transition metal ions and ferrous cyanide ions ($[\text{Fe}(\text{CN})_6]^{4-}$), resulting in significant capacity improvements. The as-prepared $\text{Na}_2\text{Ni}_x\text{Mn}_y\text{Fe}(\text{CN})_6$ electrode behaves a good reversible capacity (150 mAh g^{-1}). Advancements in composite materials also contributed to PBA development, with approaches like the preparation of PB/ MoS_2 -based nanocomposites^[20] offering superior surface areas and electrochemical performance. Innovative structural designs, including architectures with large cavities and multilayer shells, alleviated volume expansion and optimized interfacial properties, leading to enhanced initial capacity and cycling stability.

Further innovations in composition and synthesis techniques have propelled PBA research forward. In 2018, Chen and colleagues introduced a novel architectural design for PBAs,^[21] featuring large cavities and multilayer shells, as cathode material for SIBs. This innovative design aimed to alleviate volume change and optimize interfacial properties, resulting in materials with an impressive initial capacity of 123 mAh g^{-1} and exceptional cycling life. Furthermore, in 2019, Aifantis et al.^[22] proposed a concentration-gradient composition, $\text{Na}_x\text{Ni}_y\text{Mn}_{1-y}\text{Fe}(\text{CN})_6 \cdot n\text{H}_2\text{O}$, through a facile co-precipitation process. This approach was targeted at addressing mechanical degradation and enhancing the cycling stability of PBA cathodes. The composition was engineered so that the nickel concentration progressively rose from the core to the outer layer of the particle, offering improved structural integrity and prolonged cycling performance.

In recent years, there has been a notable shift in research focus towards fresh synthesis modification and structural optimization strategies for PBAs. Brezesinski's group introduced a high entropy (HE) approach in 2020,^[23] aiming to substantially enhance the electrochemical properties of PBAs. By embedding five unique metals that are all nitrogen-bound at the same site within the crystal framework, they increased the configurational

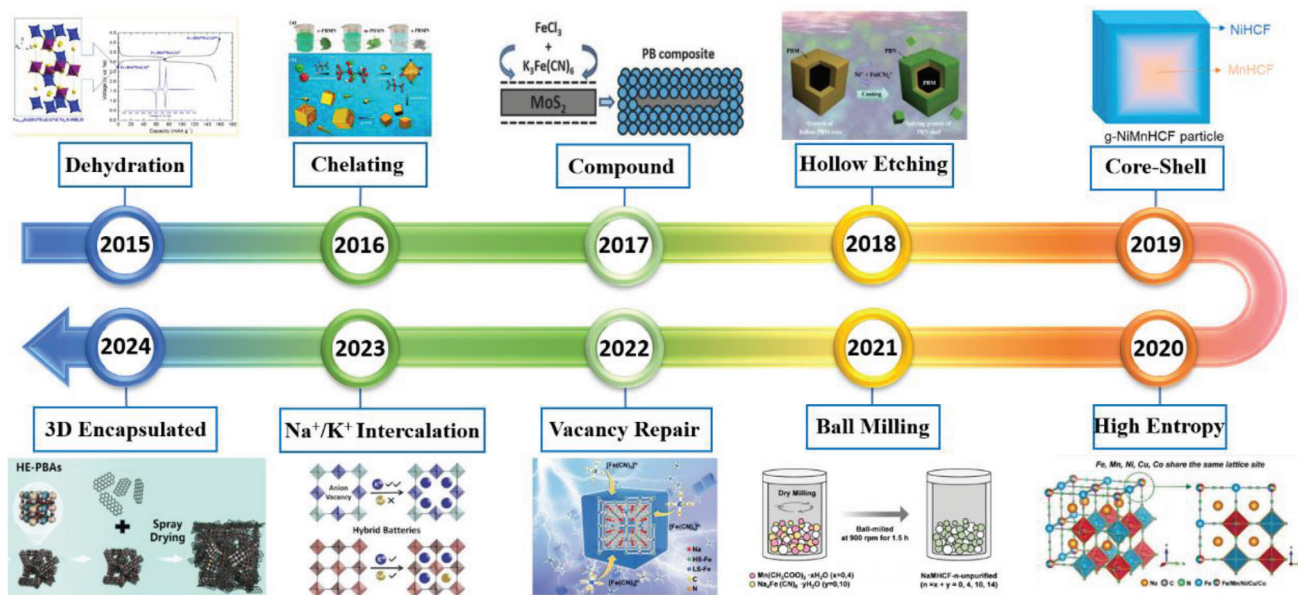


Figure 1. The development process of PBAs in SIBs. 2015: Reproduced with permission.^[18] Copyright 2015, American Chemical Society. 2016: Reproduced with permission.^[19] Copyright 2016, American Chemical Society. 2017: Reproduced with permission.^[20] Copyright 2017, Wiley-VCH. 2018: Reproduced with permission.^[21] Copyright 2018, Wiley-VCH. 2019: Reproduced with permission.^[22] Copyright 2019, American Chemical Society. 2020: Reproduced with permission.^[23] Copyright 2020, Wiley-VCH. 2021: Reproduced with permission.^[24] Copyright 2021, Elsevier. 2022: Reproduced with permission.^[25] Copyright 2021, Springer Nature. 2023: Reproduced with permission.^[26] Copyright 2023, Wiley-VCH. 2024: Reproduced with permission.^[27] Copyright 2024, The Royal Society of Chemistry.

entropy beyond 1.5R and presented a quasi-zero-strain reaction mechanism. Building upon configuration entropy strategy, in 2021, Hu and colleagues, in their study,^[24] developed a mechanochemical method that does not require solvents to synthesize monoclinic $\text{Na}_{1.94}\text{Mn}[\text{Fe}_{0.99}(\text{CN})_6]_{0.95} \cdot \Upsilon_{0.05} \cdot 1.92\text{H}_2\text{O}$ (“ Υ ” denotes empty spaces in NaMnHCF crystals where neither crystalline water nor metal atoms are present). This process involved adjusting the amount of crystal water in the precursor materials. Specifically, they reduced interstitial water content through elevated drying temperatures, enhancing the material’s properties. Subsequently, in 2022, Huang and co-workers introduced strategies for post-synthetic repair and in-situ vacancy correction to produce high-quality FeHCF using a highly concentrated solution of $\text{Na}_4\text{Fe}(\text{CN})_6$.^[25] Their approach markedly reduced vacancy defects and strengthened the structural integrity, thereby suppressing parasitic reactions and activating capacity from low-spin Fe in FeHCF . In 2023, Xu et al.^[26] further advanced PBAs’ performance by comparing two K-PBA cathodes with various vacancy contents. They demonstrated that introducing anion vacancies maximized K-ion intercalation sites and enhanced K-ion diffusion within the PBAs framework. The cathode with an increased level of anion vacancy presence, KFeRT, exhibited superior rate capacity and cycle life compared to the KFe60 cathode. Continuing this trajectory, in 2024, Liu et al.^[27] combined the benefits of the HE strategy and the 3D confinement effect that arises from the carbon wrapping (CW). They synthesized unique HE-PBAs encapsulated by three-dimensional carbon (HE-PBAs@C). This innovative structure ensured inherent stability, promoted accelerated Na^+ diffusion, enhanced electronic conductivity and reduced lattice distortion due to the 3D confinement effect.

3. Crystal Structure and Charge Compensation mechanism of Prussian Blue Analogues

3.1. Insights into the Crystal Structure of Prussian Blue Analogues

3.1.1. Crystal Structure Evolution and Electrochemical Responses

PB initially synthesized in the early 18th century, is a mixed-valent coordination polymer with the broad chemical composition $\text{A}_x\text{Fe}^{(1)}[\text{Fe}^{(2)}(\text{CN})_6]_{1-y}\Upsilon_y \cdot z\text{H}_2\text{O}$.^[28] This structure features iron (Fe) ions in both divalent and trivalent states, alternating within the framework through connections with cyanide ($-\text{C}\equiv\text{N}-$) bonds. The “A” in the formula represents alkali metal ions or guest ions that can be incorporated into PB’s crystal structure.^[29] The variable “x” in the formula changes based on the $\text{Fe}^{(1)}$ and $\text{Fe}^{(2)}$ ’s valence states.^[30] PBAs represent a broad category of compounds that are derived from PB by substituting the metal elements, resulting in the generalized formula $\text{A}_x\text{M}^{(1)}[\text{M}^{(2)}(\text{CN})_6]_{1-y}\Upsilon_y \cdot z\text{H}_2\text{O}$. In this formula, $\text{M}^{(1)}$ and $\text{M}^{(2)}$ stand for different transition metals that exhibit various spin states. Notably, $\text{M}^{(1)}$ is referred to as a high-spin species that bonds to the cyanide ligands through the nitrogen (N) atom, whereas the low-spin $\text{M}^{(2)}$ species connects via the carbon (C) atom of the ligand.^[31] Among these, Metal Hexacyanoferrates (MHCFs), denoted as $\text{A}_x\text{M}^{(1)}[\text{Fe}(\text{CN})_6]_{1-y}\Upsilon_y \cdot z\text{H}_2\text{O}$, have attracted significant attention within the energy storage community.

The crystal structure of PB and PBAs can transform among cubic, monoclinic, and rhombohedral phases, influenced by several factors, including the quantity of crystal water molecules, the type of guest cations, and the variety of transition-metal

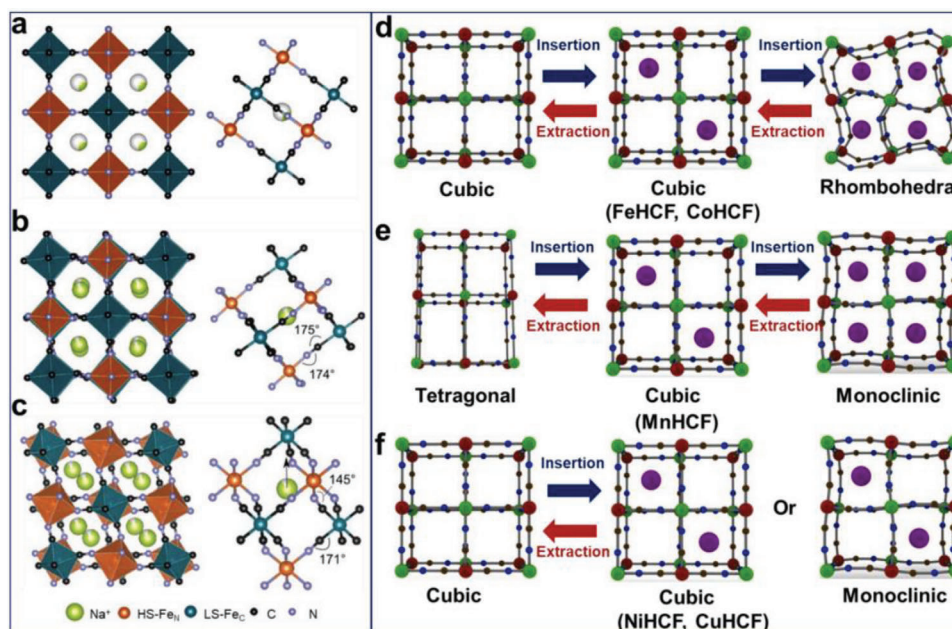


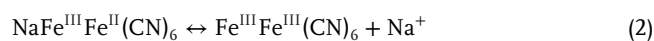
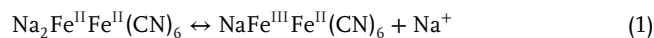
Figure 2. Local structures of PB with a) cubic, b) monoclinic, and c) rhombohedral phase. Structure evolution of d) FeHCF and CoHCF, e) MnHCF, and f) CuHCF and NiHCF induced by guest cations insertion/extraction. Reproduced with permission.^[50] Copyright 2022, Elsevier.

species.^[32,33] Typically, Fe-based Hexacyanoferrates (FeHCF) are found in a cubic phase (Figure 2a).^[34–36] However, changes in the concentration of guest cations can increase Coulombic interactions with nitrogen atoms, leading to lattice expansion.^[37] Specifically, for Sodium FeHCF (Na_xFeHCF), when the sodium content (x) exceeds 1.5, the uneven electron distribution from transition-metal ions causes varying electron shielding effects. This uneven distribution can trigger a phase shift from cubic to monoclinic, accompanied by a 6.5% expansion in the unit cell's volume (Figure 2b).^[38] Additionally, the removal of crystal water molecules reduces Pauli repulsion within the structure, facilitating a phase transition from monoclinic to rhombohedral with greater distortion (Figure 2c).^[18] This behavior is not exclusive to Na_xFeHCF ; Na_xMnHCF and Na_xCoHCF also exhibit similar phase transitions, influenced by sodium ion and water molecule content.^[39] ZnHCF stands out among PB/PBAs due to its unique structural formula and behavior;^[40] it transitions from a cubic phase at a specific hydration level to preferring a tetrahedral coordination absent in the cubic framework when dehydrated, as zinc favors tetrahedral coordination with nitrogen (ZnN_4).^[41,42] Electrochemical reactions further reveal the structural dynamics of these compounds (Figure 2d). FeHCF and CoHCF generally transition between cubic and rhombohedral phases.^[43,44] Conversely, MnHCF undergoes a more complex transition from monoclinic to cubic and then to tetragonal phase due to Jahn-Teller distortion affecting Mn-N6 octahedra (Figure 2e).^[45] Meanwhile, NiHCF and CuHCF, show minimal structural distortion during electrochemical processes, either slightly distorting to a monoclinic structure or exhibiting no phase transition at all (Figure 2f).^[46,47] For compounds containing multiple valent ions, a biphasic transition from a cubic phase to a monoclinic phase typically occurs in the presence of more than one active redox couple. In contrast, PB/PBAs featuring a single active redox pair are generally less

susceptible to phase transitions. Interestingly, the structural evolution of ZnHCF is significantly influenced by the concentration of the aqueous electrolyte, shifting from rhombohedral to cubic in low-concentration electrolytes due to increased solubility.^[48] In highly concentrated electrolytes, ZnHCF retains its rhombohedral phase without transitioning.^[49]

3.1.2. Redox Mechanisms Relevance and Significance Clarification

PB and PBAs serve as exemplary cathode materials due to their unique open-framework structure, characterized by extensive channels that enable the reversible insertion and extraction of a wide array of guest cations, including those that are hydrated. This adaptability is largely attributed to the 3D framework of PB/PBAs, which incorporates significant interstitial spaces— $\approx 4.6\text{\AA}$ in size.^[28] These spaces are large enough to accommodate the radius of most hydrated cations, as illustrated in Figure 3a, allowing for a diverse range of electrochemical interactions within the material. Theoretically, when both metal sites, $\text{M}^{(1)}$ and $\text{M}^{(2)}$, within the PB/PBA framework are capable of undergoing redox reactions, the material can host two guest cations per unit formula. This capability potentially endows PB/PBAs with a specific capacity of about 170 mAh g^{-1} . Using an FeHCF-based cathode as a case study, the underlying reaction mechanism can be outlined in the following manner:



As illustrated in Figure 3b, cathode materials featuring a single active redox site demonstrate a singular pair of anodic/cathodic

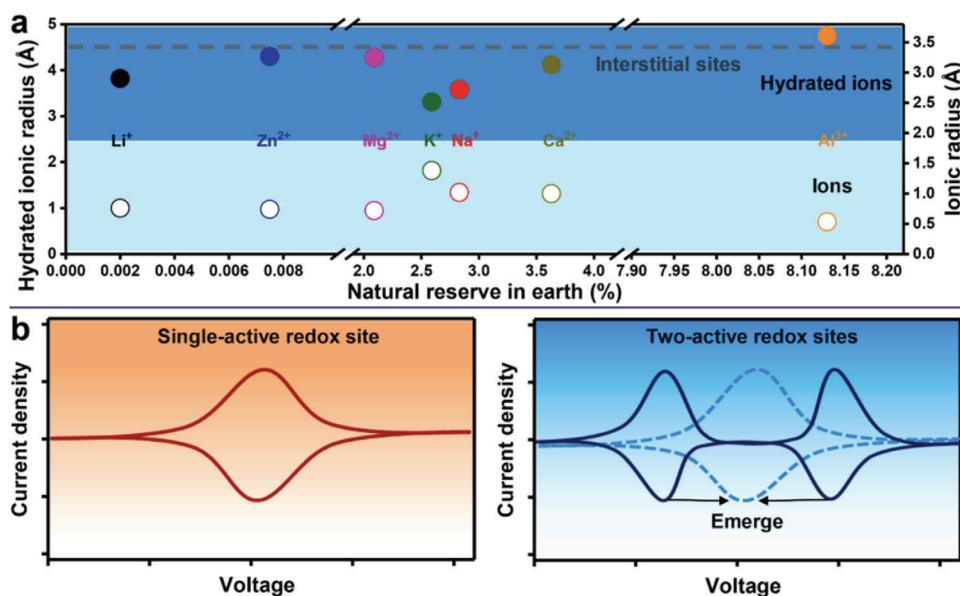


Figure 3. a) Natural reserves of metals in earth and their corresponding (hydrated) ionic radius. b) Schematic CV curves for the PB/PBAs with single- and two-active redox sites. Reproduced with permission.^[50] Copyright 2022, Elsevier.

reaction peaks. In contrast, materials equipped with dual active redox sites typically exhibit two pairs of redox peaks. This differentiation arises due to the combined effects of the ligand field and the standard redox potentials of the involved metal ions.^[51] In some instances, the two redox peak pairs might converge into a singular pair. A case in point is MnHCF, where the low-spin Fe sites coordinated to carbon in a strong ligand field manifest a higher redox potential for, while the high-spin Mn sites in a weaker ligand field reduce the Mn²⁺/Mn³⁺ redox potential. This juxtaposition results in comparable potentials for both the Fe²⁺/Fe³⁺ and Mn²⁺/Mn³⁺ sites, culminating in a singular pair of redox peaks. However, the introduction of interstitial water molecules can alter this balance by weakening the ligand field, thus potentially reinstating the distinct appearance of two redox peak pairs.^[33,39] Nevertheless, it's critical to acknowledge that PB/PBAs with two active sites often undergo more pronounced volume change during cycling. These changes can detrimentally impact the long-term cycle stability and performance of the electrodes.^[50]

3.1.3. Redox Mechanisms Deciphering: Single Electron Transfer, Two-Electron Transfer

The specific capacity achieved by early reported PBAs cathode is mostly related to single electron transfer mechanisms. Cui et al. initially reported a cubic-phase K_{0.6}Ni_{1.2}Fe(CN)₆·3.6H₂O (NiHCF) cathode, even after cycling at 8.3 C for 5000 cycles, this material showed no significant capacity decay, indicating its excellent rate performance and cycle stability.^[52] Another cubic-phase K_{0.9}Cu_{1.3}Fe(CN)₆ (CuHCF) material demonstrated good rate performance and cycle stability, highlighting the versatility of PBAs as cathodes for secondary batteries.^[53] Han et al. synthesized a low-strain material (SC-NiHCF) for SIBs through a secondary crystallization self-repair mechanism, and the corre-

sponding crystal structures of SC-NiHCF and CP-NiHCF are depicted in **Figure 4a**.^[54] The prepared defect-free material features cation-disordered sites and larger host sites, effectively preventing volume distortion during the insertion/extraction processes. Therefore, the as-prepared SC-NiHCF underwent a reversible phase transition from cubic to monoclinic phase, as confirmed by in situ X-ray diffraction (XRD) measurement (Figure 4b). Additionally, as depicted in Figure 4c,d, a specific capacity of 83 mAh g⁻¹ at an 8.0 mA g⁻¹ can be observed based on the redox couple of low spin FeLS(C), with a 93.3% capacity retention after 4000 cycles at 400 mA g⁻¹. To further enhance the capacity achieved by single electron transfer, Mai et al.^[55] performed surface etching on the rhombohedral hexagonal structure Na_{0.96}NiHCF·1.02H₂O (NiHCF-cube) to prepare a new Na_{1.11}NiHCF·0.71H₂O (NiHCF-etch) cathode with more sodium storage sites. The etched material behaved a high specific capacity of 90 mAh g⁻¹ (1.1C, 1C = 90 mA g⁻¹) and the solid-state diffusion of Na⁺ within electrodes typically follows an external-to-internal pathway. To fully utilize all reaction sites within the NiHCF-cube, Na⁺ ions must traverse a considerable distance from the surface to the center, resulting in diminished reactivity in the central region. Conversely, in the case of the NiHCF-etch, Na⁺ ions only need to diffuse over a significantly shorter distance to occupy all available insertion sites, thereby facilitating access to a larger proportion of reaction sites, including those in the central area (Figure 4e). Zhao et al.^[56] synthesized a superior high-rate and highly stable monoclinic nickel hexacyanoferrate Na_{1.48}Ni[Fe(CN)₆]_{0.89}·2.87H₂O (NiHCF-3). Density Functional Theory (DFT) calculations revealed that the doping of Ni caused deformation in NiHCF-3. This not only enhanced the framework's conductivity but also improved the electrochemical activity of Fe, resulting in exceptional rate performance in the monoclinic phase (Figure 4f).

To overcome the capacity limitation imposed by single electron transfer, recent research endeavors have focused on facilitating the involvement of a greater number of redox centers

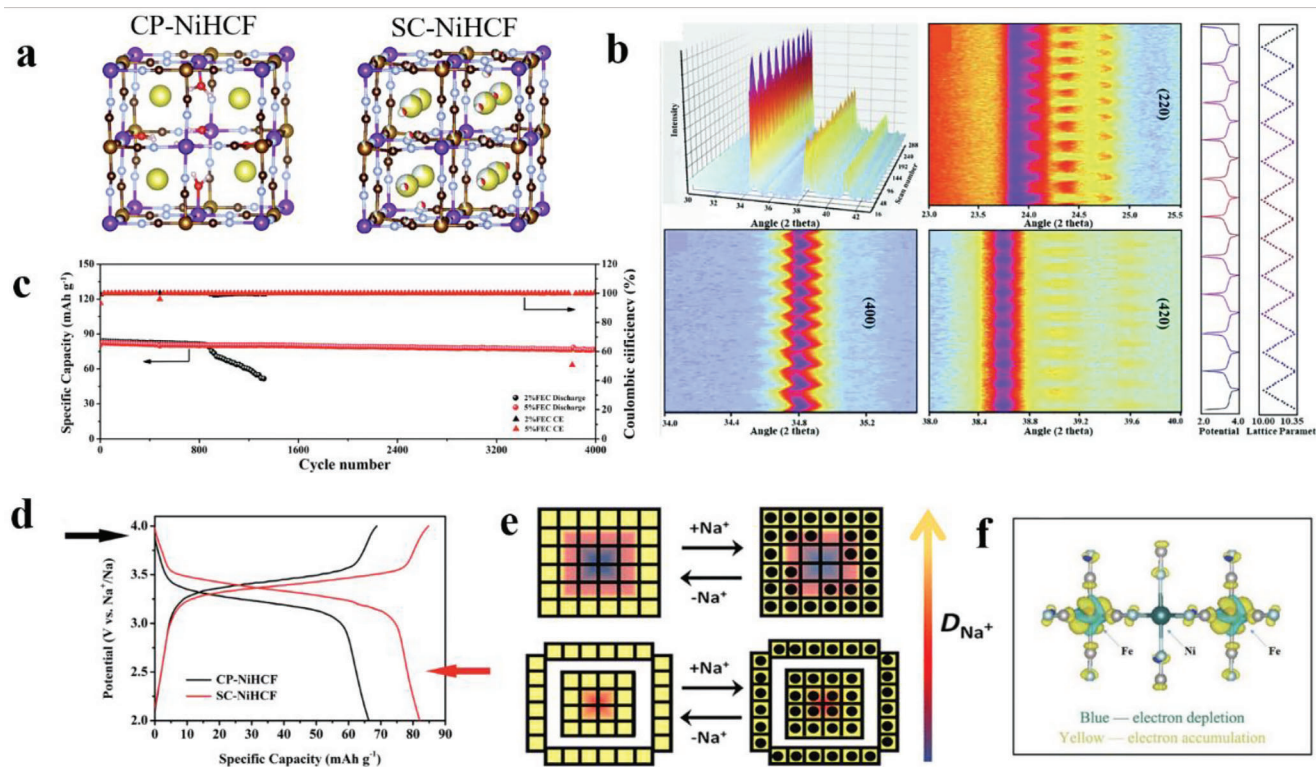


Figure 4. a) Ball and stick pattern of CP-NiHCF and SC-NiHCF electrode. b) In situ XRD analysis of SC-NiHCF under cycling at a current density of 40 mA g^{-1} . c) Long-term cycling performance of SC-NiHCF in different electrolytes. d) Charge/discharge voltage profiles of CP-NiHCF and SC-NiHCF at a current density of 0.1 C ($1 \text{ C} = 80 \text{ mA g}^{-1}$). Reproduced with permission.^[54] Copyright 2021, The Royal Society of Chemistry. e) Outside-in diffusion route of Na^+ in NiHCF-cube and NiHCF-etch. Reproduced with permission.^[55] Copyright 2017, American Chemical Society. f) Geometry optimized structure of monoclinic NiHCF, and the isosurface of the charge density difference with an identical distortion. Reproduced with permission.^[56] Copyright 2018, Wiley-VCH.

in the reaction, positioning PBAs as potential candidates for SIB cathodes with a 2 Na^+ insertion capacity. Goodenough et al. reported a series of $\text{KMFe}(\text{CN})_6$ ($\text{M} = \text{Ni, Zn, Fe, Mn, and Co}$) cathodes for SIBs, among which $\text{KFeFe}(\text{CN})_6$ (FeHCF) possessed two charge-discharge plateaus ($2.97/2.92 \text{ V}$ and $3.69/3.58 \text{ V}$ vs Na^+/Na), corresponding to the high-spin $\text{N-Fe}^{3+}/\text{Fe}^{2+}$ and low-spin $\text{C-Fe}^{3+}/\text{Fe}^{2+}$ redox reactions; thus this material provide a discharge specific capacity of 100 mAh g^{-1} at $\text{C}/20$.^[57] In addition, Guo et al.^[58] synthesized a high-quality $\text{Na}_{0.61}\text{Fe}(\text{Fe}(\text{CN})_{6})_{0.94}$ (HQ-NaFe) cathode material using a single iron source, which showed a discharge specific capacity of 170 mAh g^{-1} (25 mA g^{-1}), fully utilizing the double-electron transfer of the PB framework. Manganese-based PB materials (MnHCF) possess both $\text{N-Mn}^{3+}/\text{Mn}^{2+}$ and $\text{C-Fe}^{3+}/\text{Fe}^{2+}$ active sites, offering advantages in both high capacity and high voltage platforms, which make them competitive cathodes for SIBs. However, the Jahn-Teller effect of Mn^{3+} often leads to structural degradation during the electrochemical process, bringing about poor cycle stability. Moritomo et al.^[59] reported a $\text{Na}_{1.32}\text{Mn}[\text{Fe}(\text{CN})_{6}]_{0.83} \cdot 3.5\text{H}_2\text{O}$ thin film electrode material prepared by electrodeposition. Two charge-discharge platforms were observed at $3.42/3.12 \text{ V}$ and $3.89/3.73 \text{ V}$ versus Na^+/Na , corresponding to the $\text{N-Mn}^{3+}/\text{Mn}^{2+}$ and $\text{C-Fe}^{3+}/\text{Fe}^{2+}$ redox reactions. Nevertheless, the cycling life is unsatisfactory, thereby these kinds of cathodes need to be further modified to enhance their performance. Peng et al.^[60] synthesized ellipsoidal MnHCF-S-170 particles with a particle

size distribution (PSD) of 30 nm . Through scanning electron microscope (SEM) analysis, it was confirmed that all components of MnHCF-S-170 were evenly dispersed within the particles (Figure 5a). As presented in Figure 5b, MnHCF-S-170 exhibited a distinctive monoclinic crystal structure, while MnHCF-L synthesized through water-based coprecipitation displayed a typical cubic crystal structure. Furthermore, the discharge capacity of MnHCF-S-170 reached 164 mAh g^{-1} , closely approaching its theoretical capacity. Conversely, the capacity of MnHCF-L decreased to 135 mAh g^{-1} due to the loss of electrochemical oxidation sites associated with $[\text{Fe}(\text{CN})_6]^{4-}$ in the crystal structure (Figure 5c). Jiang et al.^[61] reported a cubic-phase $\text{Na}_x\text{MnFe}(\text{CN})_6$ (C-MnHCF) cathode material using sodium citrate as a chelating agent. C-MnHCF showed no phase transition during sodium storage (Figure 5d), exhibiting an initial discharge specific capacity of 120 mAh g^{-1} at 25 mA g^{-1} . The cubic C-MnHCF , characterized by its high structural symmetry, exhibits robust structural stability throughout the repeated insertion and extraction of Na^+ ions.

3.2. Na^+ Diffusion Mechanism of Prussian Blue Analogues

The concentration of migrating ions plays a substantial role in shaping the crystal structure and dictating the electrochemical reaction mechanism of PBAs. Depending on the number of Na^+

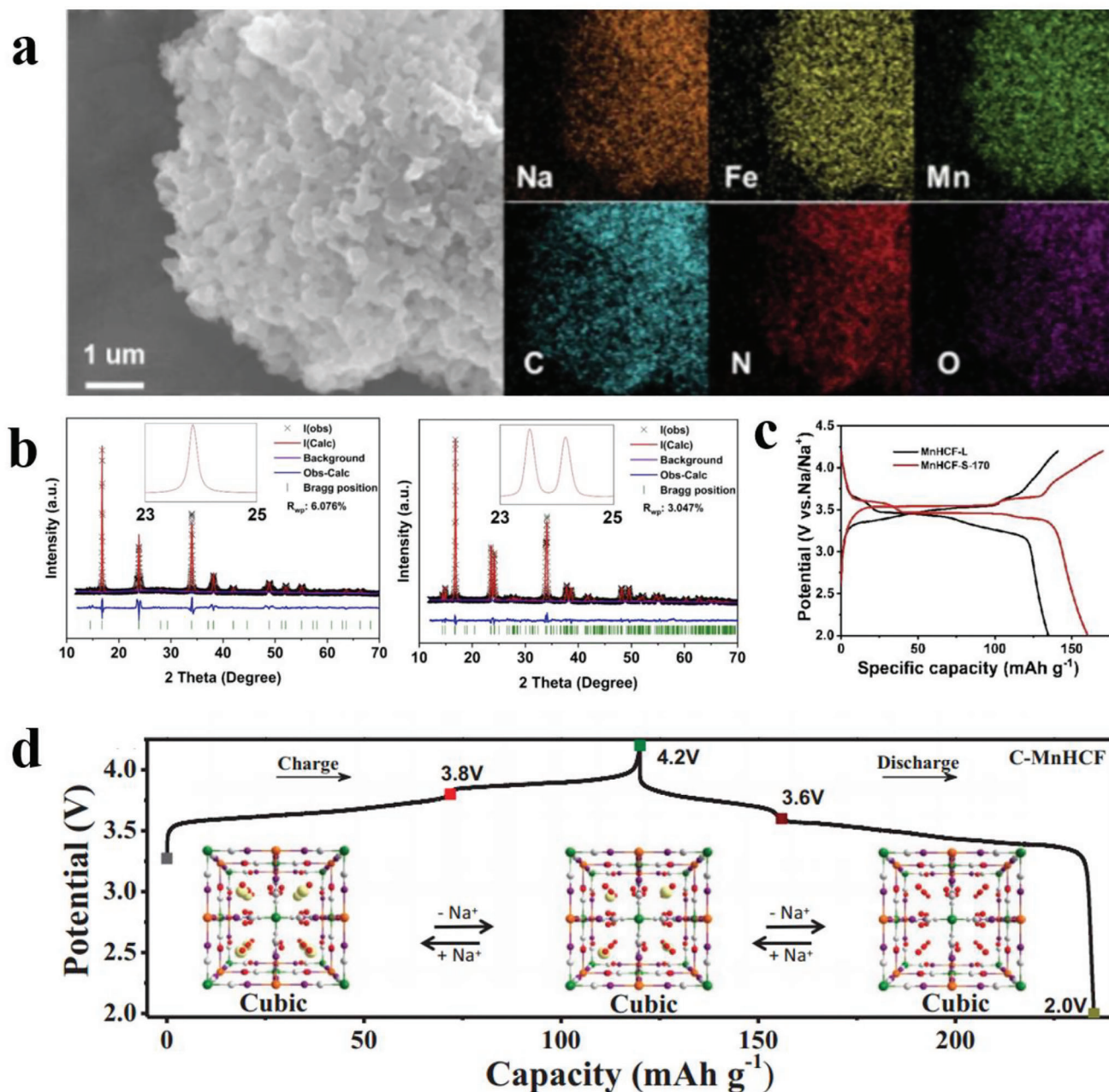


Figure 5. a) SEM image and corresponding elemental mapping images, b) Rietveld refinements of the cubic MnHCF-L and monoclinic MnHCF-S-170. c) Charge/discharge profiles at a current density of 10 mA g^{-1} . Reproduced with permission.^[60] Copyright 2022, Wiley-VCH. d) Galvanostatic charge/discharge profiles and schematic illustration of structural evolution of C-MnHCF. Reproduced with permission.^[61] Copyright 2020, Wiley-VCH.

ions present, PBAs can be classified into three distinct categories: Na-free ($x = 0$), Na-poor ($0 < x < 1$), and Na-rich ($1 \leq x \leq 2$) phases.^[62] The crystal structures of PBAs are further subdivided into cubic, monoclinic, tetragonal, hexagonal and rhombohedral forms, corresponding to changes in the content of Na⁺ ions. The cubic phase transforms to monoclinic, tetragonal and hexagonal when the Na⁺ ions content achieves a critical value of 1.6, with the presence of water molecules.^[63] Subsequently, as the Na⁺ ion content continues to rise and water molecules are progressively eliminated, rhombohedral PBAs are obtained. This sequential

transformation of crystal structures is governed by the sustained increase in Na⁺ ion content and the successive removal of water molecules.^[64–66]

3.2.1. Unveiling Na⁺ Diffusion Mechanism

The volume changes induced by Li⁺ insertion/extraction processes are well-recognized factors contributing to structural degradation in LIB research. This effect could be even more

detrimental due to the larger size of Na^+ ions, causing structural instability. To mitigate mechanical stress and maintain the structural integrity of PBAs in SIBs, Guo and colleagues^[58] employed a strategy involving the introduction of electrochemically inactive metal elements into crystal structure. Specifically, they substituted equimolar Fe^{2+} ions with sluggish Ni^{2+} ions to produce a zero-strain NaNiFe-PBA ($\text{Na}_{0.84}\text{Ni}[\text{Fe}(\text{CN})_6]_{0.71}$). This material demonstrated remarkable stability, with negligible (<1%) changes in lattice parameters observed during Na^+ insertion/extraction cycles. The “zero-strain” characteristic contributed to excellent cycling stability, with a capacity retention of 99.7% over 200 cycles and high Coulombic efficiency nearing 100%. The stable electrode/electrolyte interface within this zero-strain framework prevented ongoing breakage and reformation of the unstable solid electrolyte interphase (SEI), thus markedly improving the efficiency of charging and discharging processes. Similarly, Choi et al. pursued a similar approach by synthesizing $\text{Na}_2\text{ZnFePBA}$ ($\text{Na}_2\text{Zn}_3[\text{Fe}(\text{CN})_6]_2 \cdot x\text{H}_2\text{O}$), where the redox-capable Fe component was substituted by the electrochemically inert Zn element.^[67] This $\text{Na}_2\text{ZnFe-PBA}$ framework, featuring enlarged ionic channels, aimed to suppress volume change arising from Na^+ insertion/extraction and curb the decline in capacity due to lattice fracture. Furthermore, copper hexacyanoferrate^[68] that prepared via a solution precipitation, was studied as cathode for SIBs. The introduction of Cu enhances the cyclic stability of the material, exhibiting a capacity of 44 mA h g^{-1} at a current density of 20 mA g^{-1} , matching the one-electron redox capacity of the $\text{Fe}^{3+}/\text{Fe}^{2+}$ pair. However, developing a zero-strain PBA structure through minimal replacement of redox-active Fe atoms with an appropriate electrochemically inactive element continues to be a subject of ongoing investigation to study highly stable PBA frameworks without significantly sacrificing their Na^+ insertion capacities.

Several PBA compounds, exhibit a shared lattice architecture featuring two redox centers (M, Fe). This characteristic could lead to a higher capacity owing to a potential 2 Na^+ insertion mechanism. From an electrochemical perspective, these PBAs achieve a notable modification by replacing half of the $\text{Fe}^{2+}/^{3+}$ redox pairs with $\text{M}^{2+}/^{3+}$ pairs that exhibit similar redox activities. Within the range of transition metal ion redox couples, the $\text{Mn}^{2+}/^{3+}$ pair is preferred over the $\text{Fe}^{2+}/^{3+}$ duo for incorporation into the PBA structure, attributed to its affordability and reversible characteristics. Moritomo et al. synthesized a $\text{Na}_{1.32}\text{Mn}[\text{Fe}(\text{CN})_6]_{0.83} \cdot 3.5\text{H}_2\text{O}$ film electrode via electrodeposition,^[59] which showcased voltage plateaus at 3.2 and 3.6 V, indicative of the $\text{Fe}^{2+}/^{3+}$ and $\text{Mn}^{2+}/^{3+}$ redox reactions, respectively. The electrode showcased a discharge capacity of 109 mA h g^{-1} at a 0.5 C rate and a sustained capacity of 80 mA h g^{-1} at a 20 C rate, benefiting from the reduced ion diffusion pathway in the $1 \mu\text{m}$ thick film. In a related study, Goodenough's team^[69] unveiled a Na-enriched, rhombohedral Mn-FePBA ($\text{Na}_{1.72}\text{Mn}[\text{Fe}(\text{CN})_6]_{0.99} \cdot 2.0\text{H}_2\text{O}$) structure demonstrating a satisfied discharge capacity of 130 mA h g^{-1} at 3.5 V, alongside impressive rate performance.

3.2.2. Characterization and Density Functional Theory

Occupation sites and migration paths play a crucial role in influencing the reaction mechanism of PBAs. To gain deeper insights

into these dynamics, advanced characterization methods such as in situ/operando X-ray absorption spectroscopy (XAS), in situ X-ray absorption near-edge structure (XANES), and pair distribution function (PDF) analysis can be employed. In situ/operando XAS techniques enable the demonstration of the local crystal structure and electronic structure of PBAs cathode materials. Meanwhile, in situ XANES provides real-time monitoring information on valence and site symmetry. More recently, PDF technology has emerged as a powerful tool for studying changes in local structure and coordination geometry at the atomic scale, making it particularly suitable for the analysis of PBAs materials.^[32] When coupled with density functional theory (DFT) calculations, these techniques can reveal variations in occupation sites based on the metal ions and specific compounds under study. For example, Na^+ ions preferred 8c sites with large cavities in Na-poor conditions, whereas in Na-rich samples, some Na^+ ions were pushed into the metastable 24d sites. Peng et al.^[65] devised a novel co-crystallization approach with the aid of chelating agents/surfactants to fabricate high-quality ternary metal $\text{Ni}_x\text{Co}_{1-x}[\text{Fe}(\text{CN})_6]$ PBAs. The introduction of inert metal Ni aimed to mitigate capacity decay resulting from excessive lattice distortion, thereby enabling these PBAs to exhibit adjustable charge/discharge depth limitations. DFT calculations offer insights into the underlying mechanism of Na^+ transport within the PBA. **Figure 6a** illustrates four potential Na^+ interstitial sites, labeled as 8c, 24d, 32f(n), and 32f(c) using Wyckoff notations per cubic unit cell, in which 8c provides the largest available space, while 24d provides the smallest. DFT calculations reveal that in CoFe-PBA , site 24d exhibits the lowest binding energy (E_b), indicating a preference for Na^+ occupation. Taking into account the symmetric nature of the PBA framework, the pathways for Na^+ diffusion are divided into two main categories: (1) The movement of Na^+ ions via an S-shaped path that avoids the adjacent body's central point (Figure 6b). (2) Na^+ traverses the body center along an axis (Figure 6c). Comparative analysis of these pathways suggests that Na^+ diffusion along the S-shaped route entails a lower energy barrier, making it more favorable (Figure 6d,e). The plentiful presence of 24d sites in the PBA structure promotes an even three-dimensional distribution of Na^+ and reduces activation energy via cooperative movements, enhancing Na^+ diffusion. A minimal diffusion barrier is vital for rapid Na^+ transport, significantly influencing the rate capability of cathode materials in SIBs.

4. Challenges and Improvement Strategies in Sodium-Ion Batteries

4.1. Challenges for Synthesis

PBAs materials are commonly synthesized through a rapid precipitation process, which can introduce defects and vacancies into the crystal lattice, notably $[\text{Fe}(\text{CN})_6]^{4-}$ vacancies. Although these vacancies can enhance ionic conductivity to some extent, their occupation by water molecules may lead to structural collapse and hinder ion migration during cycling. Moreover, the low sodium content in the framework further hinders their practical application.

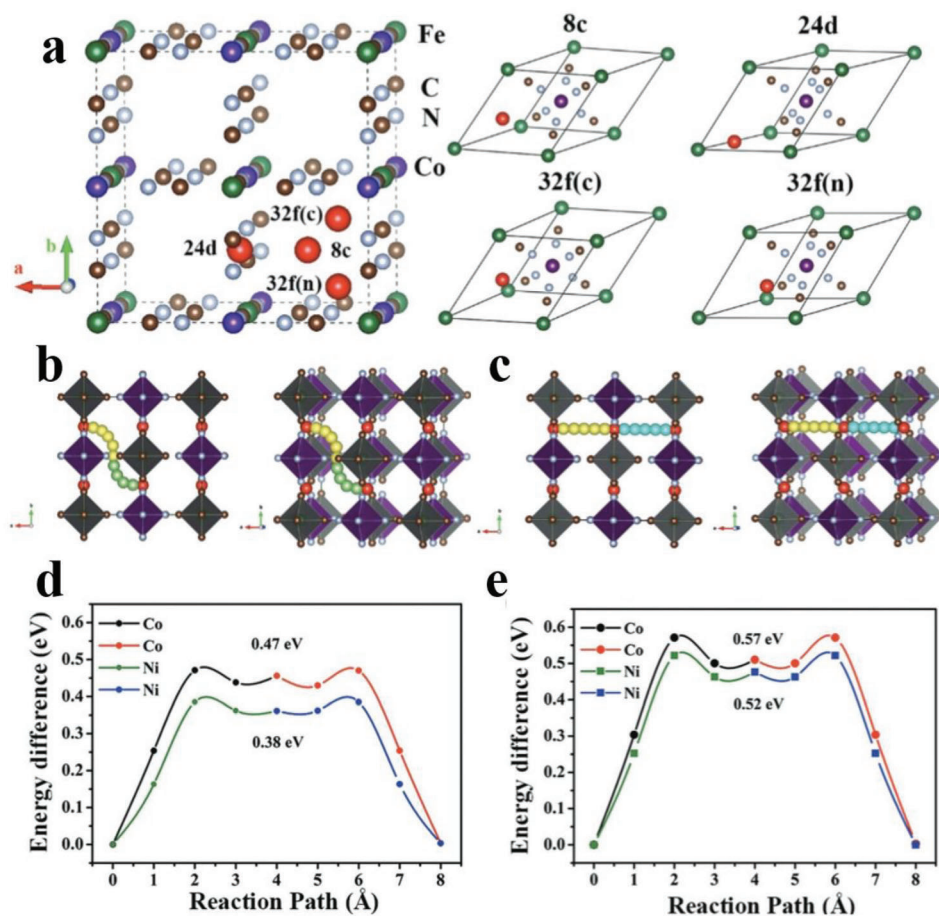


Figure 6. a) Primitive cells and crystal structure of HQ-NiCoFe with the four possible interstices of 8c (body-centered), 24d (face-centered), 32f(n), and 32f(c) (displaced from 8c sites toward N-coordinated corner), 32f(c) (displaced from 8c sites toward C-coordinated corner). b, c) Front views and corresponding side views of two possible Na⁺ migration paths, respectively. d, e) Corresponding migration energy of the above two paths. Reproduced with permission.^[65] Copyright 2018, Wiley-VCH.

4.1.1. Defects and Vacancies

Since PBAs are typically prepared through a straightforward and swift precipitation process, a large number of defects and vacancies inevitably emerge within the open crystal framework structure.^[12,32] Defects in PBAs crystals encompass deviations or losses of atomic positions, which can arise from impurities, ion loss, atomic dislocation, and other factors. Vacancies, on the other hand, specifically denote unoccupied atomic positions within the crystal lattice. In PBAs, vacancies mainly refer to the position of [Fe(CN)₆]⁴⁻ loss. Both defects and vacancies may have important effects on the performance of PBAs, such as affecting ion conductivity and crystal stability.^[70] However, a notable drawback associated with a high vacancy rate in the structure is the heightened risk of crystal instability and possible structural failure during repeated cycles. Moreover, these empty spaces are prone to water molecule absorption, which hinders Na⁺ ion movement and results in slower reaction dynamics. Furthermore, the presence of [Fe(CN)₆]⁴⁻ vacancies makes it challenging to fully activate the Fe-LS (low spin Fe) redox reaction, ultimately leading to a reduced sodium storage capacity.

4.1.2. Crystalline Water

Within the original PB configuration, featuring a 3:4 ratio of Fe²⁺ and Fe³⁺ sites, the manifestation of crystalline water, namely coordinated water, introduces 25% [Fe(CN)₆]⁴⁻ vacancies.^[71,72] Other water molecules in this structural framework can be classified into adsorbed and interstitial water, each exerting distinct effects.^[6,32] Various analytical techniques can be employed to characterize adsorbed water, interstitial water, and crystalline water in PBAs. These include thermogravimetric analysis (TGA), nuclear magnetic resonance (NMR), and Fourier transform infrared spectroscopy (FTIR). TGA allows for quantitative analysis of adsorbed water and crystalline water content by monitoring the sample's mass change during heating. NMR provides insights into the position and environment of water molecules within the crystal structure, facilitating differentiation between different types of water. FTIR spectroscopy distinguishes between different types of water molecules based on their respective stretching and bending vibration modes. Furthermore, online monitoring techniques such as in situ heating Raman spectroscopy, in situ heating X-ray diffraction, and thermogravimetric-mass spectrometry (TG-MS) can be utilized to investigate the dynamic

evolution of crystalline water removal in PBAs. Water that is absorbed or zeolitic, found either on the surface or within the gaps of the lattice, can be readily eliminated. However, water that is coordinated tends to form strong bonds with Fe ions, making its removal difficult and affecting the electronic configurations of adjacent Fe ions or the $[\text{Fe}(\text{CN})_6]^{4-}$ complexes.^[32] The consequential presence of crystalline water within PBAs strongly affects their electrochemical performance.^[39,51] Especially in well-studied SIBs with organic electrolyte systems, crystalline water within PBAs acts as an “invisible killer,” which is accompanied by the synergistic effect of absorbed and zeolitic water, contributing to electrolyte deterioration, electrode damage and undesirable side reactions. Excessive water not only obstructs redox-active sites and traps Na^+ ions but also contributes to the structural breakdown of the PBA framework.^[73] Addressing these challenges involves refining the PBAs preparation process and adopting strategies such as direct vacuum drying, as demonstrated by Goodenough’s team, to obtain dehydrated $\text{Na}_2\text{MnFe}(\text{CN})_6$.^[39]

4.1.3. Low Sodium Content

$\text{Na}_2\text{FeFe}(\text{CN})_6$ is viewed as a promising option for Na-rich cathode materials, thanks to its optimal composition, offering a theoretical sodium storage capacity of $\approx 170 \text{ mAh g}^{-1}$. This capacity is based on the extraction of two Na^+ ions for every formula unit. In full cells based on PBAs, the peak capacity is significantly determined by the cathode’s initial sodium content, especially when paired with a commercial hard carbon anode. Therefore, high sodium content holds great significance for the commercialization of PBAs electrodes. The amount of sodium in the precursor solution and the valency of transition metals, particularly iron (Fe), are critical in determining the sodium levels in the crystalline structures of the synthesized PBA cathodes. For instance, Wang et al.^[74] synthesized a hierarchical Na-rich $\text{Na}_{1.58}\text{Fe}[\text{Fe}(\text{CN})_6]_{0.92}$ through by adding excess NaCl into the precursor solution to enhance the sodium concentration, which is vital to ensure the occupation of more sodium ions in the host frameworks. Sodium citrate here is not only used as a common extra sodium source like NaCl, but also functions as a chelating agent. Furthermore, through the protection of an inert N_2 atmosphere, Guo et al. reported a FeHCF cathode with high sodium content, applying ascorbic acid (VC) as a reducing agent has been shown to be effective. Researchers discovered that VC, in combination with N_2 gas, could significantly inhibit the oxidation of $\text{Fe}^{2+}/[\text{Fe}^{\text{II}}(\text{CN})_6]^{4-}$ to $\text{Fe}^{3+}/[\text{Fe}^{\text{III}}(\text{CN})_6]^{3-}$, resulting in the incorporation of 1.63 sodium ions per chemical formula unit.^[75]

4.2. Synthesis Modification

Taking into account the critical interplay among vacancies, water occupation, and sodium content from a materials synthesis viewpoint, improving the crystallinity is beneficial for producing high-quality PBAs. This improvement leads to fewer $[\text{Fe}(\text{CN})_6]^{4-}$ vacancies, reduced water content, and increased sodium reserves. Typically, defect and lattice vacancies could be restricted or repaired by optimizing synthetic methods and post-synthesis heat treatment processes. For example, introducing surfactants such

as polyvinylpyrrolidone (PVP) reduced defects and coordinated water formation by lowering surface tension; controlling crystallization rates by adding chelating agents could suppress defect formation; removing crystal water through heat treatment improved the material’s initial capacity, cycling stability, and rate capability. Furthermore, by creating a sodium-rich environment and employing chelating agents, sodium ion content in the final product has been increased, thereby enhancing the sodium storage performance of PBAs materials.

4.2.1. Vacancy Removal and Repair

In traditional hydrothermal or precipitation synthesis processes, incomplete crystal growth often leads to a high number of vacancies filled with coordinated water, creating defect structures within the 3D open framework. These defects can compromise structural integrity, decrease Na^+ storage sites, lower electronic conductivity, and slow down Na^+ diffusion. Efforts to reduce $[\text{Fe}(\text{CN})_6]^{4-}$ defects focus on two main strategies. Optimization of synthesis is the first strategy. By refining synthesis methods, researchers have successfully reduced vacancy defects and coordinated water.^[58,76–78] Guo et al.^[58] produced high-quality PBAs nanocrystals with minimal zeolite water and vacancy defects, achieving a specific capacity of 170 mAh g^{-1} , exceptional cycle stability, and nearly perfect Coulombic efficiency. Jiang et al.’s^[77] low-vacancy CuHCF, synthesized using a strategy that utilizes ethanol to prevent Cu^{2+} and water coordination, showed improved rate performance and activated additional redox reactions at lower voltages. Secondly, use of surfactants, like polyvinylpyrrolidone (PVP), can reduce surface tension and consequently the number of vacancies and coordinated water,^[79–82] promoting the growth of high-quality crystals and providing chemical protection against etching.^[80] Despite these advancements, eliminating vacancies remains a challenge due to low yields from these methods. Therefore, research has shifted towards $[\text{Fe}(\text{CN})_6]^{4-}$ vacancy repair strategies, including ball-milling and high-concentration solution treatments, to improve material quality and electrochemical performance.^[38,83] For example, $\text{NaFeFe}(\text{CN})_6$ prepared via ball-milling showed repaired vacancies and enhanced properties.^[25] Similarly, advanced FeHCF materials were developed to reduce and repair vacancies, (Figure 7a–d) showing improved stability and capacity. (Figure 7e,f). Moreover, Wang et al.^[84] explored using sodium ferrocyanide in high-concentration sodium chloride solutions to address surface Mn^{2+} vacancies in cathode materials, enhancing specific capacity and cycling life by preventing Mn^{2+} dissolution and promoting vacancy filling (Figure 7g–i). These comprehensive approaches highlight the multifaceted strategies employed to address challenges in PBA materials for energy storage applications.

4.2.2. Heat Treatment

Hexacyanoferrates (HCFs) inherently incorporate water by reason of their specific crystal structures, generating a high water reserve reaching 10–15 wt% in cubic or monoclinic HCFs. Despite water molecules being stable within the HCF structure under

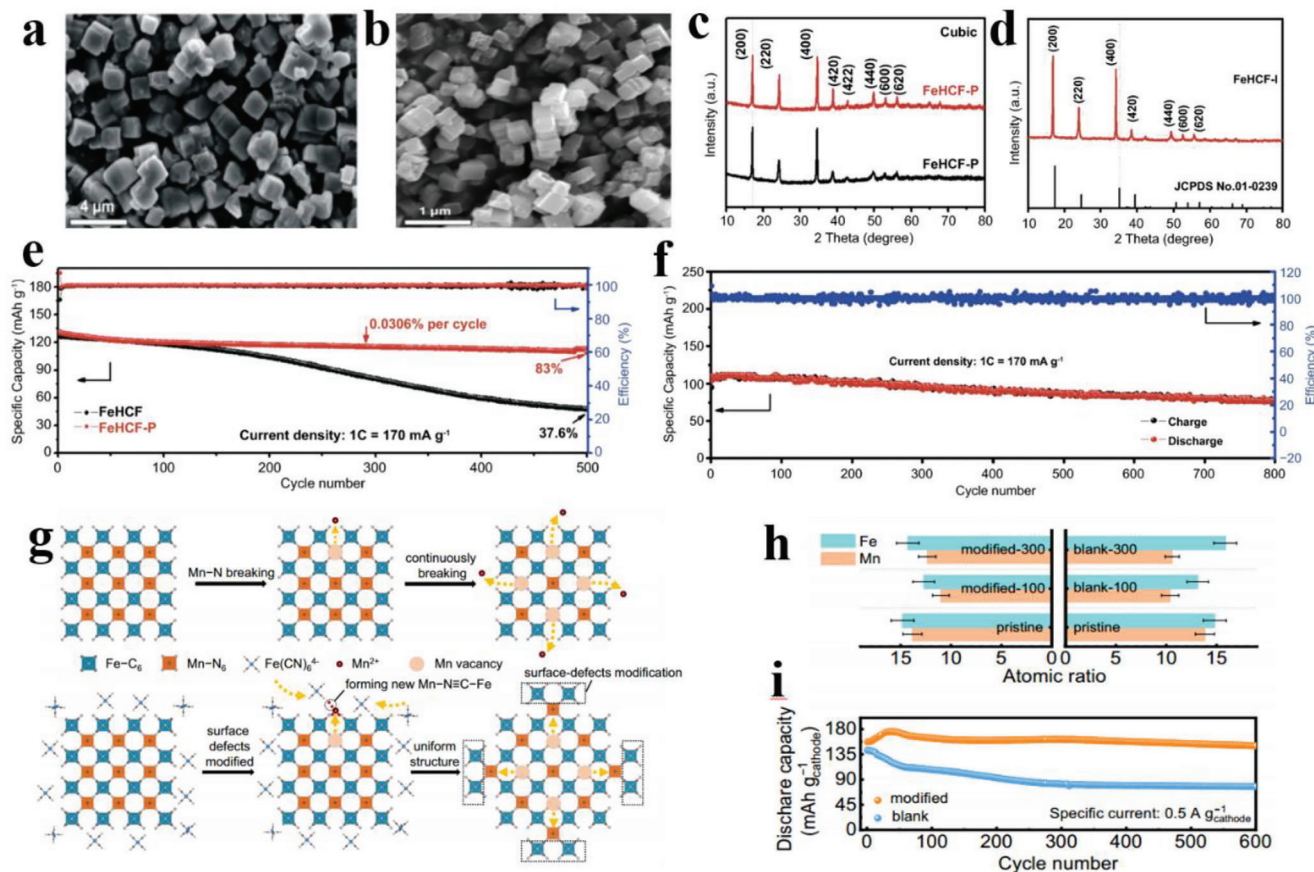


Figure 7. SEM images of a) FeHCF-P and b) FeHCF-I. XRD patterns of c) FeHCF-P and d) FeHCF-I. e) Cycling performance of FeHCF and FeHCF-P samples under 1 C. f) Cycling stability of FeHCF-I at 10 C. Reproduced with permission.^[25] Copyright 2021, Springer Nature. g) The Schematic illustration of Mn dissolution process and the cation-trapping process. h) The atomic ratio of Mn and Fe in the cycled cathode in the blank (17.6 M NaClO₄) and modified (17.6 M NaClO₄ + 0.33 M Na₄Fe(CN)₆) electrolytes as determined by ex situ EDS. i) Comparison of the cycling performance of PTCd||NaFeMnF in the blank and modified electrolytes at 25 °C. Reproduced with permission.^[84] Copyright 2023, Springer Nature.

typical conditions, electrochemical cycling can trigger their dissociation, bringing about irreversible water extraction and subsequent serious battery performance degradation. Theoretical calculations further revealed the binding energy of crystal water in NaMnHCF framework undergoes a fast decline from 0.8 to 0.1 eV after Na⁺ extraction.^[85] Heating NaFeHCFs in a monoclinic form also resulted in a transformation to a rhombohedral structure through thermal dehydration.^[86–87] Chou et al.^[76] used a simple heat treatment method to remove water from iron-based PBAs and this cathode displayed different crystal structure when calcinating at 40 °C (pristine trigonal phase), 270 °C (cubic and trigonal mixed phases), and 320 °C (new trigonal phase), respectively). More interestingly, the dehydrated samples exhibited a notable increase in capacity from 50 mAh g⁻¹ to 96 mAh g⁻¹ compared to the untreated samples (Figure 8a). Crystal water within the framework structure can be eliminated via high-temperature treatment. Nevertheless, it will inevitably cause structural collapse when the dehydration temperature is too high, generating gas by-products and leading to a rapid decline in electrochemical performance. Therefore, it is of great significant to find a suitable dehydration temperature to remove the water molecules.

4.2.3. Na-rich Composition and Chelating Agent Treatment

Creating a Na-rich environment in an aqueous precursor solution proves convenient for obtaining Na-rich PBAs cathodes. Therefore, to improve the Na⁺ content in the host structure of the PBAs materials, excess sodium-containing raw materials such as NaCl is frequently used, aiding in the formation of a Na-rich environment and reducing the [Fe(CN)₆]⁴⁻ vacancies and crystal water. Chou's group introduced a large number of NaCl and polyvinylpyrrolidone (PVP) into a Na₄Fe(CN)₆ solution containing hydrochloric acid, obtaining Na-rich Na_{1.56}Fe[Fe(CN)₆]·3.1H₂O with decreased [Fe(CN)₆]⁴⁻ vacancies and coordinated water at 80 °C.^[79] Additionally, sodium citrate, Na₂EDTA, sodium oxalate, sodium pyrophosphate, and other chelating agents, not only improve the crystallinity and morphology of HCF but also serve as sodium source to increase the sodium content within the framework of the final product. Dou et al.^[88] prepared a highly crystalline and sodium-rich PB using trisodium citrate as a chelating agent and sodium source. The PB-S1 sample, generated with a small amount of chelating agent, exhibited a cubic phase, while the PB-S3 sample, using large amounts of chelating agents, showed a rhombohedral

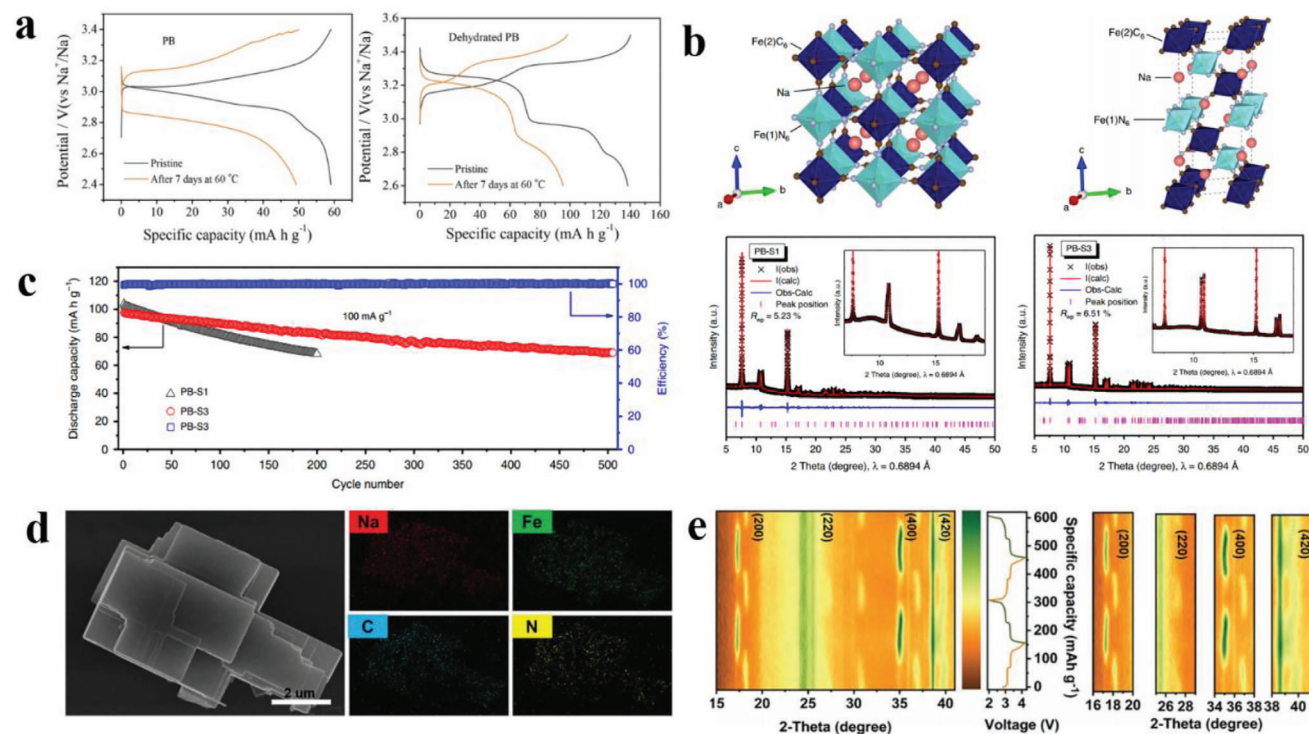


Figure 8. a) Capacity storage performance of the pristine and dehydrated PB after 7 days at 60 °C. Reproduced with permission.^[76] Copyright 2022, Wiley-VCH. b) Structure and Rietveld refinement of cubic (PB-S1) and rhombohedral (PB-S3) samples. c) Cycling performance of PB-S1 and PB-S3, Reproduced with permission.^[88] Copyright 2020, Springer Nature. d) SEM image and EDS elemental mapping of FeHCF, e) In situ XRD patterns of FeHCF with corresponding charge/discharge curves and 2D contour images. Reproduced with permission.^[89] Copyright 2023, Wiley-VCH.

phase and demonstrated superior cycling stability (Figure 8b,c). Another monoclinic iron-substituted nickel-rich PBAs^[89] cathode (H-PBA) using Na₂EDTA as a chelating agent via a hydrothermal method can hold nearly 1.5 Na⁺ ions within its host structure. The crystallization-controlled approach with pyrophosphate decelerated the crystal growth process and improved the defect content within the crystal framework of iron-based PBAs, which helps generate a sodium-rich rhombohedral phase with high crystallinity and uniform elements distribution (Figure 8d).^[89] Furthermore, in situ XRD revealed a highly reversible three-phase transition process from a cubic phase to a rhombohedral phase and subsequently to a monoclinic phase (Figure 8e).

4.3. Structural Stability Challenges in Cycling

PBAs materials face challenges such as irreversible phase transitions, lattice distortion, and the Jahn-Teller effect during charging/discharging process, which not only result in changes in lattice volume but also induce significant structural stress, affecting the structural stability and electrochemical properties. Crystalline water within PBAs can adversely affect electrochemical performance, especially in organic electrolyte systems. Considerable attention has been paid to deeply investigating the nature of these hazardous challenges in order to find effective strategies to further ameliorate the performance of PBAs and address these shortcomings.

4.3.1. Irreversible Phase Transitions

Generally, the PBAs cathodes, which exhibit five main kinds of phases like cubic,^[58,90] monoclinic,^[9,56] tetragonal,^[18] hexagonal,^[91] and rhombohedral phases.^[89] During the Na⁺ insertion/extraction processes, phase transitions often occur. These transformations highlight the diversity of structural phases encountered, where cubic, monoclinic, tetragonal, and hexagonal phases show a deficiency in Na, in contrast to the Na-enriched rhombohedral phase. Additionally, crystal phase transitions inevitably generate large volume changes and serious structural stress, which are heavy blows to structural stability. For the development of highly stable PBA cathodes, it is essential to ensure reversible phase transitions that involve minimal volume changes and low variations in crystal stress. This approach is critical in maintaining structural integrity and ensuring long-term cycling stability in SIBs.

4.3.2. Lattice Distortion

The lattice strain of PBAs merit in-depth investigation, particularly substantial stress variations in the lattice structure induced by Na⁺ insertion during cycling, which can result in alterations in lattice parameters, distortions of unit cell, and deviations from ideal atomic positions.^[87] In specific studies, researchers commonly employ various characterizations like X-ray diffraction, neutron diffraction, and electron microscopy to detect

the properties of lattice distortion. Boström et al.^[92] observed that defects exert significant influence on both lattice distortion and phase transition behavior, utilizing variable-pressure X-ray and neutron diffraction techniques. The main causes of lattice distortion include temperature changes, uneven material composition, external stress, and other factors. These factors lead to changes in the positions of atoms within the crystal, resulting in lattice distortion. Lattice distortion can lead to a decrease in the mechanical properties of materials, changes in electronic structure, and even the fracture or failure of the crystal.

4.3.3. Jahn–Teller Effect

Typically, the Jahn-Teller effect is a phenomenon of structural distortion in crystals, typically occurring around TM ions with partially filled d or f electron shells. This effect arises from the arrangement of outer electrons and the disruption of symmetry, leading to a distortion in the crystal structure. If a molecule or ion has incompletely filled electron shells, it tends to distort the lattice to reduce the energy caused by the asymmetry of electrons. This distortion stabilizes the electron distribution of the molecule or ion, thereby reducing the total energy. For PBAs materials, the Jahn-Teller effect often occurs in crystal structures containing TM ions such as manganese. During the insertion/extraction of sodium ions, the crystal structure of this kind of material undergoes distortion. This distortion may lead to crystal structure instability, affecting electrochemical performance and cycling life. MnHCF undergoes three phase transitions during Na⁺ (de) insertion processes, involving monoclinic (Na₂MnFe(CN)₆), cubic (NaMnFe(CN)₆), and tetragonal (MnFe(CN)₆) phases.^[18] The shift from a cubic to tetragonal phase is associated with structural deformation caused by the Jahn-Teller distortion of Mn-N₆ octahedra, which also causes the dissolution of Mn²⁺ ions. Therefore, it is paramount to suppress this phenomenon to realize the prolonged cycling life of PBAs cathodes.

4.3.4. Parasite Reactions and Transition Metal Dissolutions

During the charging process, PBAs electrodes operating at low potentials may undergo electrolyte reduction reactions, resulting in the production of partial C₂H₄ and C₂H₆. This reaction leads to the influx of a considerable amount of interstitial water into the electrolyte solution. Conversely, when operating at high potentials, PBAs electrodes may generate CO₂ and H₂.^[23] Specifically, CO₂ is produced from oxidation reactions of organic carbonate electrolytes at the cathode, while the release of H₂ stems from reduction reactions of interstitial water at the anode. The generation of these by-product gases may give rise to serious safety concerns, such as battery swelling or even explosion, posing serious risks. Concurrently, due to the cycling-induced damage and collapse of crystal structures, certain transition metal ions like Fe²⁺ and Mn²⁺ inevitably undergo dissolution effects.^[84,89]

4.4. Structure Optimization Strategies

To address the aforementioned challenges, several strategies have been explored for structure optimization. These include

surface coating, structure design, element substitution, and the high-entropy strategy. Surface coating and structure design involve creating suitable core-shell structures, controlling lattice matching between the core and shell, and introducing protective surface layers to improve cyclic stability. Element substitution aims to mitigate volume expansion and lattice distortion by incorporating inert TM elements into the PBA structure, thus enhancing the crystal stability and increasing the capacity. The high-entropy strategy means creating high-entropy alloy structures composed of multiple elements to increase the configurational entropy of the crystal, thereby ameliorating structural stability. These strategies have shown positive effects on enhancing the performance of PBAs to varying degrees, offering valuable insights for research and applications in SIBs.

4.4.1. Structure Design and Surface Coating

Mechanical deterioration in cathode substances poses a considerable technical obstacle, manifesting through localized cracking, creation of fresh reactive interfaces, and increased resistance to electronic conduction, all of which contribute to diminished capacity and battery malfunction. The main factors driving the mechanical weakening of PBAs cathode substances include uneven stress due to phase changes, volumetric swelling, and the emergence of voids during Na⁺ insertion or removal. Creating a suitable core-shell structure has demonstrated to be a beneficial strategy for enhancing electrochemical performance and the advantages are outlined as follows: Well-designed shells with appropriate compositions can increase Na⁺ storage sites and display good elasticity to accommodate volume changes and reduce internal stresses within the core lattice, resulting in a higher specific capacity and excellent electrochemical stability. Sun et al.^[93] successfully applied nickel hexacyanoferrate (NNiFCN) on the surface of iron hexacyanoferrate (NFFCN) through ion exchange. The variation in electrostatic potential strength across the inner and outer layers creates an inherent electric field within the NNiFCN/NFFCN structures, aiding in Na⁺ migration and enhancing cycle durability. However, the potential of these structural benefits is not fully realized owing to inadequate lattice alignment between the core and shell, which have distinct chemical compositions. Moreover, the complexity of the synthesis steps and the lack of a comprehensive understanding of the formation mechanism present challenges. As a result, significant lattice discrepancies and the cumbersome synthesis process collectively hinder the advancement of core-shell approaches. And more research should further develop heterogeneous core-shell structures to enhance structural stability and specific capacity. Moreover, to mitigate the mechanical degradation of PBAs cathodes, Hu et al.^[22] reported a concentration-gradient g-NiMnHCF (Na_xNi_yMn_{1-y}Fe(CN)₆·nH₂O) through a co-precipitation process. This structure, with its Ni concentration gradually increasing from the core to the surface, effectively reduces the stress and damage caused by electrochemical activity during Na⁺ insertion and removal. This unique gradient prevents the cracking commonly seen in uniform samples, enhancing durability and performance. Notably, g-NiMnHCF and MnHCF exhibited 0.29% and 8.5% volume expansion, highlighting the effectiveness of the

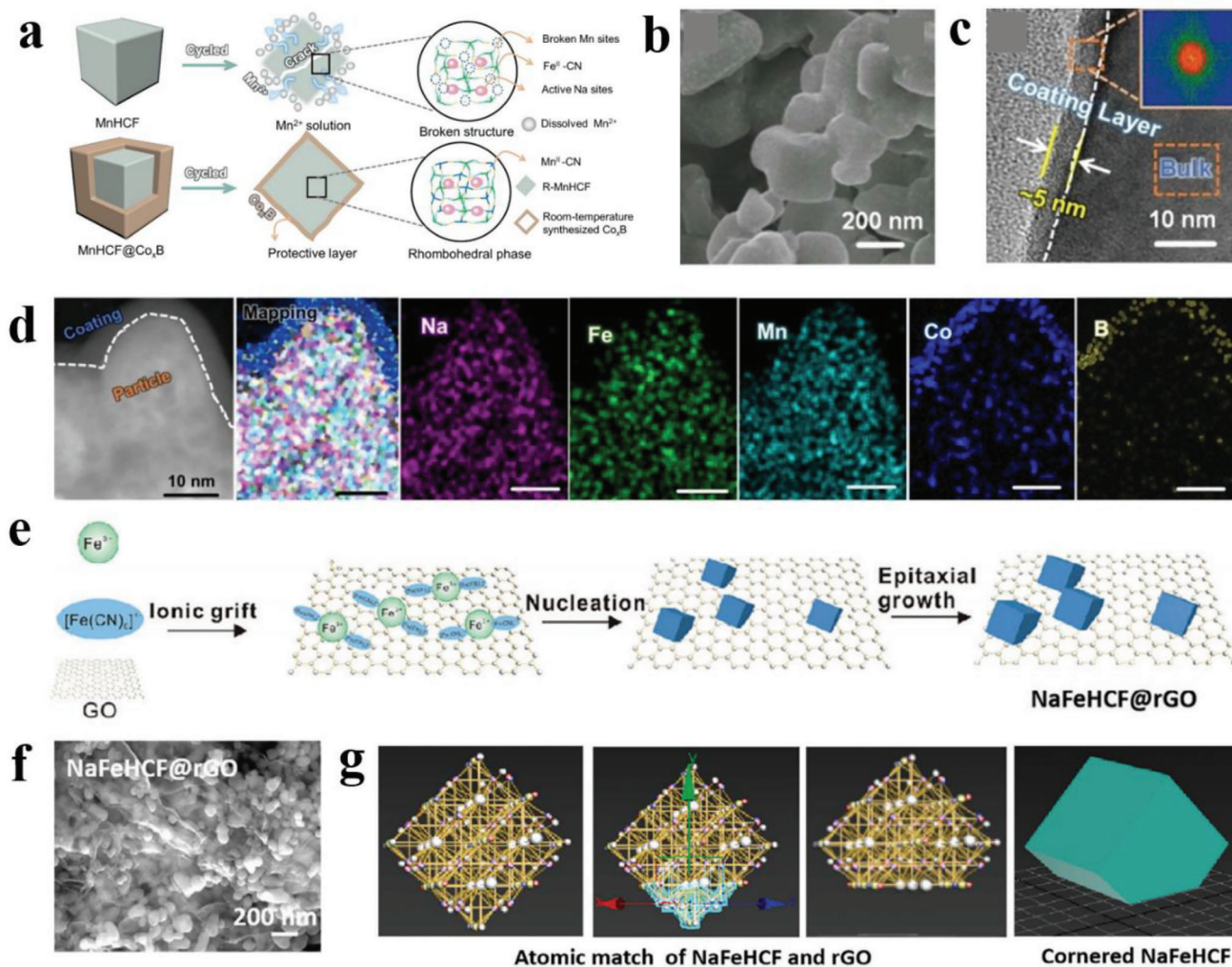


Figure 9. a) Schematic illustration of the proposed protective mechanism of Co_xB to suppress the Mn dissolution and generation of microcracks of MnHCF cathode. b) SEM and c) HRTEM images of MnHCF-5% Co_xB . d) TEM and EDS element mapping of MnHCF-5% Co_xB . Reproduced with permission.^[94] Copyright 2023, Wiley-VCH. e) The nucleation-assisted controlled crystallization process of NaFeHCF@rGO. f) SEM images of NaFeHCF@rGO. g) Morphology characteristics of NaFeHCF and NaFeHCF@rGO. Reproduced with permission.^[95] Copyright 2024, Wiley-VCH.

concentration-gradient design in improving the stability of PBAs cathodes.

Constructing composites through the protection of surface layers is a preferred strategy for mitigating volume change and reducing structural strain. These composites, formed by combining the host material with other substances like carbon-based materials and conducting polymers through physical/ chemical binding, offer several advantages: First, compounding additional materials on PBAs enhances electronic conductivity, leading to improved electrochemical performance. Second, the flexible surface layer of the composite adapts to lattice strain during Na^+ ions (de)intercalation, effectively reducing lattice disorder throughout cycling. Thirdly, the composite layer serves as a protective barrier, preventing the surface dissolution of the electrode as well as inhibiting side reactions at the interface.

For example, Hu et al.^[94] developed a room-temperature precipitation method to prepare a Co_xB protective layer on MnHCF surface. The Co_xB layer, fully enveloping the MnHCF cathode,

plays a crucial role in mitigating Mn dissolution and minimizing intragranular interfacial cracks. This protective coating acts as a stress buffer, enhancing the structural integrity and stability of the cathode material (Figure 9a). SEM images showed that the cubic structure of MnHCF was well maintained but with the formation of a relatively rough surface, indicating complete coverage of the Co_xB coating (Figure 9b). HR-TEM images displayed a uniform distribution of ≈ 5 nm amorphous Co_xB coating on the surface of MnHCF-5% Co_xB particles (Figure 9c). TEM energy dispersive spectroscopy (TEM-EDS) analysis indicated a concentration of Na, Fe, and Mn elements predominantly within the core of the MnHCF-5% Co_xB particles. In contrast, Co and B atoms were found to be enriched on the surface, highlighting the Co_xB 's even distribution as a shell covering the MnHCF particles (Figure 9d). Jiang et al.^[95] eliminated the structural defects of NaFeHCF crystals using a epitaxial nucleation-assisted crystallization method. Due to the lattice mismatch between graphene and NaFeHCF being only 4.87% (<5%), and the

-COOH, -OH, and -CH(O)CH- functional groups having electronegativity, graphene oxide could serve as a nucleation initiation and crystallization-guiding substrate for high crystalline NaFeHCF nanoparticles (Figure 9e). As shown in Figure 9f, cubic particles adhered to the graphene oxide film. This resulted in a unique single-edge-cut cubic nanocrystal morphology, significantly reducing the defect content (0.08 per formula unit) (Figure 9g). This improved lattice structure significantly boosted Na ion diffusion within the nanocrystals, leading to an exceptional rate performance of 96.8 mAh g⁻¹ at 9 A g⁻¹ (39 s, 23 228 W kg⁻¹), setting a new benchmark for PBA-based cathode materials, demonstrating its advantages as a candidate material for reliable grid energy storage in high-power SIBs.

4.4.2. Element Substitution

Element substitution is a widely employed strategy for enhancing the electrochemical characteristics of PBAs through modifying the composition and proportions of elements. This approach involves introducing inert TM elements to mitigate the irreversible phase transition, restrain volume change and inhibit lattice distortion, thereby improving the stability of host lattice during electrochemical process. For A_xM[Fe(CN)₆]_{1-y}Y_y·zH₂O cases where M is Ni, Cu, or Zn, the inert N-coordinated M center, providing a low Na⁺ insertion capacity while maintaining good electrical conductivity, structural stability, and high-rate performance. Choi et al.^[67] explored the substitution of redox-reactive Fe with electrochemically inert Zn in Na₂Zn₃[Fe(CN)₆]₂·xH₂O, achieving improved Na⁺ diffusion due to enlarged ion channels, and demonstrated enhanced electrochemical performance with a reversible capacity of 56.4 mAh g⁻¹ and promising cycle durability. In cases where the metal (M) is Mn, Co, or Fe, the presence of two redox couples (Fe²⁺/Fe³⁺ and M²⁺/M³⁺) theoretically enables the accommodation of 2 Na⁺ ions per formula unit, aiming for a high storage capacity of approximately 170 mAh g⁻¹. However, practical capacities often range from 90 to 150 mAh g⁻¹ due to the suboptimal activity of Fe in low-spin states. Mn-based HCFs (MnHCF), in particular, are noted for their high initial capacity and are favored for their abundance, affordability, and synthesis simplicity. Yet, the susceptibility of Mn³⁺ to dissolve into the electrolyte due to the Jahn-Teller effect necessitates solutions to mitigate the resulting phase instabilities and structural distortions. Introducing multiple metallic dopants into the N-coordinated metal centers has emerged as an effective strategy to address these challenges, enhancing the electrochemical performance. Notably, Moritomo et al.^[96] improved the stability and activated the high-voltage redox activity of Mn-HS in Na_{1.6}Mn[Fe(CN)₆]_{0.9} by doping with transition metals such as Fe, Co, and Ni.

Moreover, Ma et al.^[97] have advanced the performance of PBAs by incorporating Fe vacancies and Cu doping within their structural framework. The creation of Fe vacancies not only introduces additional Na⁺ storage sites but also facilitates Na⁺ diffusion kinetics, leading to a significant capacity enhancement of ≈ 164 mAh g⁻¹, closely matching the theoretical capacity at lower current densities (Figure 10a). The strategic addition of Cu dopants further reinforces the structural integrity of the PBAs, thereby

improving their cycling stability. The study noted that the resulting PBA(Cu)YFe cathodes retained a cubic particle morphology, albeit with increased particle sizes ranging from 300 to 400 nm, indicating that Cu doping promotes the growth of more regular and larger particles. X-ray diffraction (XRD) analysis confirmed that the crystal structure remains unchanged by Fe vacancies and Cu substitution, maintaining a face-centered cubic symmetry akin to the Fm-3m space group. Through thermogravimetric analysis (TGA), the PBA(Cu)YFe samples demonstrated superior thermal stability between 30 and 400 °C compared to their PBA and PBA YFe counterparts, as evidenced by less weight loss, attributing to the enhanced structural fortitude provided by Cu doping. Despite a slight reduction in capacity due to the decrease in active sites following Cu incorporation, the electrochemically inert nature of Cu doping plays a pivotal role in stabilizing the framework, effectively mitigating performance degradation over repeated cycling. In consequence, the PBA(Cu)YFe electrode behaved a superior cycling capacity retention of 78.5% after 200 cycles at 500 mA g⁻¹, whereas PBA YFe just maintained 48.4% of its initial capacity (Figure 10e), indicating a significant improvement in cycling stability with Cu doping. Furthermore, Sun et al.^[98] proposed another new strategy, i.e., adding multivalent cations in the electrolyte, to enhance the structural stability of PBAs and improve the diffusion rate of sodium ions. To be more specific, during charge and discharge processes, Ba²⁺ could be inserted into the PBA lattice through in situ electrochemical reactions. Acting as “defenders”, Ba²⁺ maintained the stability of the framework, preventing residual moisture from entering the lattice (Figure 10f,g). DFT calculations showed that the energy required for Na⁺ diffusion to adjacent interstitial sites was significantly reduced after Ba²⁺ insertion into the framework, thereby enhancing Na⁺ diffusion and reaction kinetics (Figure 10h).

4.4.3. High Entropy Strategy

In recent years, introducing high entropy into the positive electrode materials of SIBs has emerged as a new trend. Elevating the configurational entropy above 1.5R in disordered multicomponent systems is generally believed to induce a high entropy (HE) effect, enhancing the overall crystal stability of the material and inhibiting lattice distortion and irreversible phase transitions. The stabilizing characteristics of the high entropy effect further interact with doped cations, resulting in a “cocktail” effect. In the crystal structure, the positions of high-spin Fe atoms can be substituted by other TM ions with redox activity, further improving their electrochemical behavior. Increasing the configurational entropy in PBAs improves structural stability, thermal/air resistivity, and achieves highly reversible zero-strain phase conversion mechanisms. Compared to medium entropy PBAs (ME-PBA) and traditional PBAs (Fe-PBA), HE-PBAs exhibit excellent sodium storage performance and electrochemical stability when samples are prepared using a facile co-precipitation method at room temperature.^[99,100] Brezesinski's^[23] group reported a PBA cathode with a quasi-zero strain working mechanism by introducing five different transition metal elements in equimolar amounts into the crystal structure, sharing the same nitrogen coordination sites, thus increasing the system's configurational

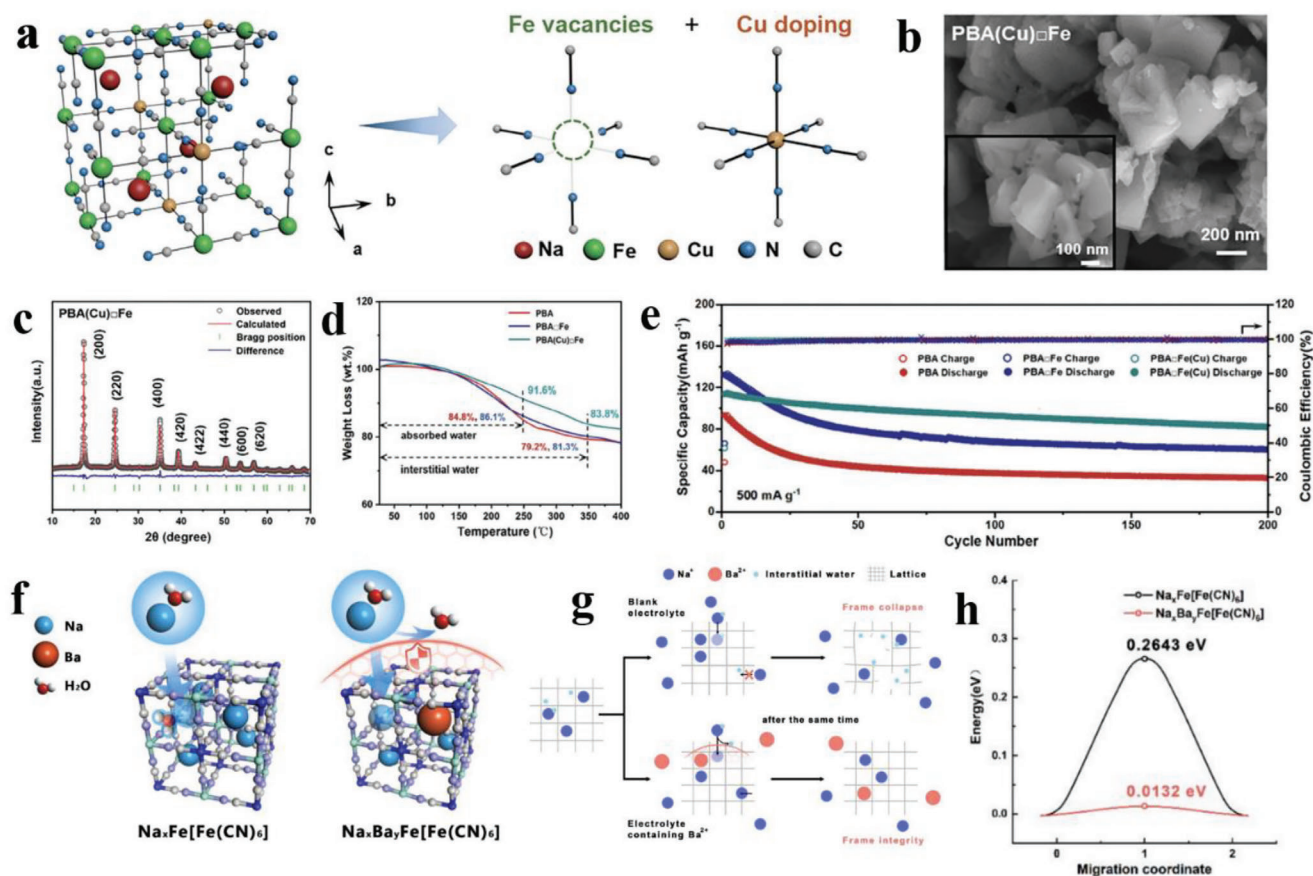


Figure 10. a) Structure diagram of PBA(Cu)Fe. b) SEM diagram of PBA(Cu)Fe. c) Rietveld refinement analysis of PBA(Cu)Fe. d) TG curve of PBA, PBA:Fe, and PBA(Cu)Fe. e) Cycling performance comparison between PBA, PBA:Fe, and PBA(Cu)Fe at 500 mA g⁻¹. Reproduced with permission.^[97] Copyright 2024, Wiley-VCH. f) Schematic illustration of the role of Ba²⁺ as a "defender" in the PBA framework. g) Schematic diagram of Ba²⁺ to prevent water molecules from entering the lattice to maintain the framework stability. h) Energy required for Na⁺ ion to move from one interstitial site ([A] site) to another adjacent interstitial site ([B] site) in the PBA framework containing Na⁺ and Ba²⁺, respectively. Reproduced with permission.^[98] Copyright 2023, Elsevier.

entropy to above 1.5R. This team also applied high entropy concept to Mn-HCF,^[101] enhancing the reversibility and mitigating the capacity decay Mn-HCF positive electrodes due to adverse structural transformations and deterioration throughout cycling cycles. The increase in entropy effectively suppresses structural revolution, significantly improving cycling stability compared to medium and low entropy MnHCFs. Chou et al.^[102] prepared HCF structures containing five metals, proving that MOFs can be applied as high entropy materials for SIBs because these cathodes exhibited an ultralong cycling life exceeding 50000 cycles and outstanding rapid charging capability. More interesting, Ting et al.^[103] found that composition element plays different roles in a HE-PBA cathode containing five metals. For instance, Cu doping effectively improves electron conductivity, while Zn doping regulates vacancy formation, and their co-doping even makes synergistic effects to adjust particle size and specific surface area.

Combining the HE with other modification strategies contributes to further ameliorated performance of PBAs cathodes. Jiang's group^[104] reported a strategy involving single crystals and HE-PBAs (SC-HEPBA) to simultaneously address the challenges

of excessive sodium storage and poor long-term cyclic stability in positive electrodes for SIBs. The HE characteristics enhance Na⁺ diffusion kinetics and effectively suppress the dissolution of TM ions, while micrometer-sized single crystals help reduce structural damage during cycling. In addition, vacancy and water content in the material framework are significantly reduced in this single crystal structure, forming a high-sodium-content monoclinic phase. Due to the synergistic effects, SC-HEPBA achieves reversible monoclinic-cubic-tetragonal phase transitions with negligible metal dissolution. Yu et al.^[105] proposed a strategy to address the challenges of low operating voltage and poor structural stability of PBAs by utilizing HE and potassium doping to construct the HE-K-PBA electrode. The crystal structure of HE-K-PBA, consisting of five TM ions (Mn, Fe, Co, Ni, and Cu) in equimolar ratios occupying nitrogen coordination sites, with low-spin Fe occupying carbon coordination, forms a three-dimensional framework (Figure 11a). The highly similar coordination environments of these component elements are confirmed by X-ray absorption spectroscopy (XAS) and extended X-ray absorption fine structure (EXAFS) (Figure 11b). In identical load and environmental scenarios, HE-K-PBA displayed

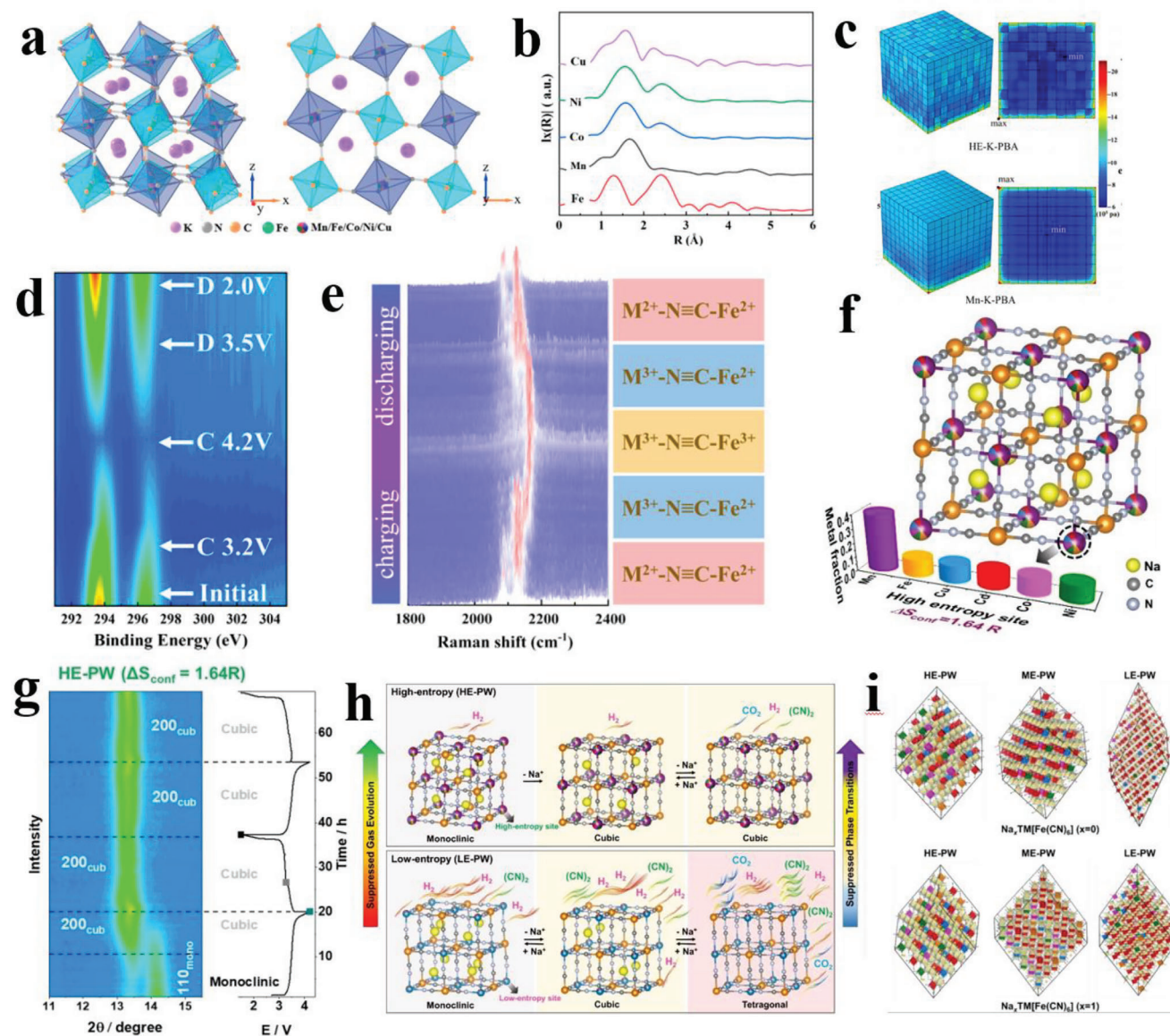


Figure 11. a) Schematic crystal structure of HE-K-PBA. b) Extended X-ray absorption fine structure (EXAFS) signals of five transition metals of HE-K-PBA. c) 3D von Mises stress distributions and corresponding ground stress distributions of HE-K-PBA and Mn-K-PBA. d) Ex situ XPS analysis of HE-K-PBA cathode during the second cycle. e) In situ Raman spectra analysis. Reproduced with permission.^[105] Copyright 2023, American Chemical Society. f) Schematic illustration of the crystal structure of HE-PW. g) Contour plots and corresponding voltage profiles for HE-PW. h) Schematic illustration of the structural evolutions and corresponding gassing behavior of HE-PW and LE-PW. i) Crystal structures of HE-PW (cubic), ME-PW (tetragonal) and LE-PW (tetragonal) in the fully charged state ($x = 0$ in $\text{Na}_x\text{TM}[\text{Fe}(\text{CN})_6]$) and corresponding structures for $x = 1$ (cubic). Reproduced with permission.^[106] Copyright 2023, Wiley-VCH.

considerably reduced maximum and minimum von Mises stresses compared to Mn-K-PBA and four other single-component PBA variants. (Figure 11c). All these contribute to building a stable structure. Ex situ XPS analysis and in situ Raman spectra demonstrated highly reversible reactions of HE-K-PBA during cycling, further confirming its excellent structural stability (Figure 11d,e). Thermal expansion simulations of HE-K-PBA during discharge showed significantly smaller average strains compared to Mn-K-PBA and the other four single-component PBAs (Co-K-PBA, Ni-K-PBA, Cu-K-PBA,

and Fe-K-PBA), indicating that the high entropy effect effectively suppresses lattice distortions during electrochemical cycling, significantly improving electrode structural stability. This is primarily attributed to the interactions between the five transition metal components. Due to its stable structure and reversible K^+ insertion, HE-K-PBA exhibited output voltage of 3.46 V, reversible capacity of 120.5 mAh g^{-1} at 0.01 A g^{-1} , and preeminent capacity retention of 90.4% after 1700 cycles at 1.0 A g^{-1} .

Another subgroup of PBAs, i.e., Prussian white cathode, has attracted considerable attention because of the rich sodium

reserves in the host structure but faces similar challenges with other PBAs electrode material. Ma et al.^[106] applied the HE strategy to monoclinic PW electrodes, synthesizing series Mn-based samples with up to 6 transition metals sharing N coordination. Local structure analysis revealed that 6 metal atoms with Mn predominating occupy the same N coordination position in 2a Wyckoff position, and Fe1 atoms coordinated with C located at the 2d position ($\text{Na}_x\text{Mn}[\text{Fe1}(\text{CN})_6]$) (Figure 11f). Compared to medium/low entropy and conventional single-metal PWs, materials composed of high entropy PWs exhibited better cycling stability. In situ XRD revealed an initial transition from monoclinic to cubic phase upon de-sodiation, followed by a solid solution behavior with minimal peak position changes. And during subsequent precipitation, the cubic phase remained unchanged, indicating a highly symmetrical structure (Figure 11g). Mechanistic studies of this strategy revealed a dual effect of high entropy in inhibiting adverse phase transitions and slowing down by-product gas generation (Figure 11h). First-principle DFT calculations on HE-, ME-, and LE-PW materials showed that, with all Na^+ ions removed (in the $\text{Na}_x\text{TM}[\text{Fe}(\text{CN})_6]$ formula with $x = 0$), the HE-PW material transitions to a high-symmetry cubic phase, whereas ME-PW and LE-PW materials favor a tetragonal structure that is more stable thermodynamically. When fully saturated with Na^+ ions ($x = 1$), a cubic phase becomes the most stable configuration for all three categories of materials (Figure 11i). Despite the multicomponent material showcasing enhanced cycle durability over traditional single and dual-component PBAs, the high-entropy approach still necessitates further investigation to fully understand its operational dynamics within this material system and its effects on the performance of batteries.

5. Summary and Outlook

5.1. Summary

PBAs have emerged as a prominent material in the realm of electrochemical energy storage, attributed to their notable advantages such as affordability, ease of synthesis, stable open framework structure, and eco-friendliness. This review has provided an in-depth analysis of the crystal structure, redox mechanism, and Na^+ diffusion mechanism integral to PBAs. Furthermore, we have thoroughly examined the challenges and obstacles that PBAs encounter in their path towards commercial application in SIBs, alongside a detailed exploration of various strategies aimed at enhancing their fundamental properties. Specifically, the issues of inherent vacancies, defects, and crystalline water, which are prevalent in the conventional coprecipitation synthesis method, have been addressed through several synthesis modifications, including vacancy remediation and heat treatment techniques. In addition to the methods outlined in this review, such as structural design and elemental substitution, further advancements are imperative to improve cycling stability, which is currently hindered by irreversible phase transitions, lattice distortions, and the Jahn-Teller effect observed during the electrochemical cycling. The review concludes by highlighting prospective directions for both laboratory research and the practical deployment of PBA materials in SIBs, setting the stage for future innovations in this field.

5.2. Outlook

5.2.1. Innovation in Synthesis Methods

While traditional methods for synthesizing PBAs offer benefits such as high yield, low cost, and straightforward processes, they also lead to significant challenges, including incomplete crystal growth and the formation of numerous vacancies and defects during the precipitation process. These issues can degrade the electrochemical performance of PBAs. To address these shortcomings, alternative synthesis strategies like ball milling, templating, hydrothermal, and electrochemical deposition have been explored, each showing promise for advancing the field.

Ball milling, in particular, has been recognized for its ability to produce highly crystalline PBAs through a one-step reaction, eliminating the need for chelating agents and excess sodium salts. This simplifies the preparation process, enhancing its potential for future commercial applications. However, PBAs cathodes prepared via ball milling tend to exhibit lower performance compared to those synthesized by co-precipitation methods. The optimization of ball milling parameters, such as time and speed, remains underexplored and necessitates further research to boost the electrochemical performance of PBAs. The hydrothermal method offers controlled synthesis under high-temperature and high-pressure conditions, allowing for precise manipulation of the morphology, size, and structure of PBAs nanoparticles. Despite its advantages in controlling synthesis parameters, the hydrothermal approach suffers from higher energy consumption, longer reaction times, lower yields, and reduced production efficiency, making scale-up for industrial production challenging. Templating methods provide meticulous control over the morphology and structure of PBAs, enabling the preparation of particles with desired shapes and sizes by selecting appropriate templates. This precision is vital for improving electrochemical performance and tailoring materials to specific practical applications. Templating results in uniform-sized and evenly distributed PBAs particles, improving material homogeneity, which positively influences the electrode surface and charge transfer rate. Nevertheless, this approach often involves more complex preparation steps and conditions, potentially increasing complexity and production costs. To surmount these obstacles and fully harness the potential of PBAs in sodium-ion batteries, ongoing innovation and refinement of synthesis methods are essential. Efforts to optimize these novel approaches will be crucial for achieving enhanced electrochemical performance and for the practical commercialization of PBAs.

Consequently, the synthesis method for PBAs cathode materials for SIBs in the future must adhere to several essential criteria to be deemed ideal: (1) Efficiency in Production: It should enable the creation of high-quality PBAs cathode materials swiftly to boost production efficiency. (2) Precision and Control: The method must allow precise control over the crystal structure, morphology, and chemical composition to tailor the electrochemical properties according to specific requirements. (3) Scalability: The synthesis approach should be adaptable to large-scale industrial production, catering to various production volumes without compromising quality. (4) Cost-Effectiveness: Utilization of readily available raw materials and equipment is crucial to keep production costs low. (5) Environmental Sustainability: It should

prioritize green synthesis techniques that minimize or eliminate environmental impact, thereby conserving resources and promoting sustainability. In summary, the synthesis approach for future PBA cathode materials ought to be efficient, precise, scalable, economical, and environmentally benign, all while ensuring the production of materials with superior electrochemical characteristics. Among the various methods evaluated, large-scale ball milling emerges as a promising direction for synthesis, offering a balance between production efficiency, quality control, and environmental sustainability. This approach aligns well with the outlined criteria, highlighting its potential as a leading method for the future development of PBA cathode materials for SIBs.

5.2.2. Cost and Security Issues

While PBAs present an economically viable option for SIBs due to their low-cost and straightforward synthesis via ambient temperature coprecipitation, their application raises pertinent cost and safety issues that necessitate careful consideration.

Cost Considerations: The affordability of PBAs is a significant advantage, yet the discussion often overlooks the broader cost implications, including raw material procurement, synthesis efficiency, and waste management. To reduce costs further, future designs of PBAs should focus on optimizing these aspects. Strategies might include sourcing cheaper raw materials, refining the synthesis process to increase yield and efficiency, and implementing waste reduction techniques. Additionally, advancements in automated production and process optimization can lead to significant economies of scale, further driving down the cost of PBAs for commercial applications.

Safety Improvements: Safety concerns with PBAs primarily revolve around the presence of cyanide groups in their structure, which pose toxicity risks. To mitigate these risks, future PBA designs could incorporate non-aqueous synthesis methods to eliminate or minimize the formation of toxic by-products such as NaCN and HCN. Solvent substitution and enhanced process safety measures, including the use of less hazardous chemicals and the development of safer reaction conditions, are also vital. Moreover, selecting compatible electrolytes and improving the sealing of battery components can prevent adverse chemical reactions, enhancing safety. Implementing thermal management and temperature control systems can further ensure safety by preventing thermal runaway during abnormal operation conditions.

Environmental and Safety Protocols: Acknowledging the environmental impact of PBAs, it is crucial to establish appropriate disposal and recycling protocols. These measures not only address the environmental concerns but also contribute to the safety profile of PBAs by ensuring that any potential hazards are effectively managed throughout the material's lifecycle.

In conclusion, while PBAs offer a cost-effective solution for SIB cathodes, addressing the comprehensive cost implications and safety concerns is essential for their sustainable commercial application. Future PBA designs should aim to lower costs through raw material and process optimization and enhance safety through innovative synthesis methods, improved material handling, and rigorous environmental protocols. Specific strate-

gies, such as automated production lines, process optimizations, material surface modifications, and the establishment of stringent monitoring systems, will be instrumental in realizing the full potential of PBAs in various applications while ensuring the production process remains both cost-efficient and safe.

5.2.3. Prospects for Commercial Application

PBAs are carving a niche for themselves as the cornerstone for cost-effective, large-scale energy storage systems, leveraging their compatibility with SIBs. The energy storage capacity of SIBs, marked at $\approx 100\text{--}150\text{ Wh kg}^{-1}$, surpasses that of lead-acid batteries and competes with some lithium iron phosphate-based batteries. A notable milestone has been achieved by CATL with its first-generation PBA-based cathode material for SIBs, boasting an energy density of up to 160 Wh kg^{-1} . This material demonstrates rapid charging capabilities, achieving over 80% capacity within just 15-minute at room temperature, and maintains 90% of its discharge capacity in cold conditions as low as $-20\text{ }^{\circ}\text{C}$. These features underscore the significant commercial potential of PBAs in the realm of SIBs. Furthermore, SIBs equipped with PBA cathodes have shown remarkable cycling stability, exceeding 2000 cycles, setting the stage for bridging the performance gap with LIBs.

To promote the commercial adoption of PBAs in SIBs, it is imperative to prioritize continuous improvement in energy density and cycling life. Enhancements in these areas are crucial for lowering the cost of electricity from energy storage facilities and fulfilling the demanding requirements of commercial-scale energy storage solutions. Advanced characterization techniques, including in situ/operando measurements, such as XRD, Raman spectroscopy, and XAS have been instrumental in shedding light on the properties of PBAs. Furthermore, the adoption of cutting-edge technologies offering higher resolution, such as solid-state nuclear magnetic resonance (NMR), aberration-corrected transmission electron microscopy (TEM), and low-temperature TEM, are paving the way for a deeper understanding of PBA.^[107] These techniques allow for the exploration of PBAs' mechanisms without altering the material structures, providing insights that are critical for optimization.

In view of CATL's success in commercializing PBAs for SIBs, the focus now shifts toward refining these applications to achieve even greater efficiency and reliability. Enhancing the synthesis process, improving material stability, and optimizing the electrochemical properties of PBAs are key areas for research and development. The goal is to approach and gradually exceed the performance benchmarks set by existing battery technologies, ensuring PBAs play a pivotal role in the future of sustainable energy storage. Through concerted efforts in research, development, and innovation, the widespread commercial application of PBAs in SIBs is anticipated to materialize in the near future, marking a significant leap forward in the quest for advanced, cost-effective energy storage solutions.

Acknowledgements

Y.X., J.X. and H.Z. contributed equally to this work. H.G. and Y.W. acknowledge the support from Open Project of State Key Laboratory of

Advanced Special Steel, the Shanghai Key Laboratory of Advanced Ferrometallurgy, Shanghai University (SKLASS 2021-04), the Science and Technology Commission of Shanghai Municipality (22010500400) and “Shanghai Pujing Program” (23PJ1402800), “Joint International Laboratory on Environmental and Energy Frontier Materials” and “Innovation Research Team of High-Level Local Universities in Shanghai” in Shanghai University.

Open access publishing facilitated by University of Wollongong, as part of the Wiley - University of Wollongong agreement via the Council of Australian University Librarians.

Conflict of Interest

The authors declare no conflict of interest.

Keywords

cathode, commercial application, improvement strategies, prussian blue analogues, sodium-ion batteries

Received: March 12, 2024

Revised: April 2, 2024

Published online: April 29, 2024

- [1] J. Chen, G. Zhang, J. Xiao, J. Li, Y. Xiao, D. Zhang, H. Gao, X. Guo, G. Wang, H. Liu, *Adv. Funct. Mater.* **2024**, *34*, 2307959.
- [2] W. Shu, J. Li, G. Zhang, J. Meng, X. Wang, L. Mai, *Nanomicro Lett* **2024**, *16*, 128.
- [3] T. Yuan, Y. Chen, X. Gao, R. Xu, Z. Zhang, X. Chen, L. Cui, *Small Methods* **2023**, *9*, 2301372.
- [4] C. Peng, X. Xu, F. Li, L. Xi, J. Zeng, X. Song, X. Wan, J. Zhao, J. Liu, *Small Struct.* **2023**, *4*, 2300150.
- [5] H.-W. Lee, R. Y. Wang, M. Pasta, S. Woo Lee, N. Liu, Y. Cui, *Nat. Commun.* **2014**, *5*, 5280.
- [6] X. Wu, Y. Ru, Y. Bai, G. Zhang, Y. Shi, H. Pang, *Coord. Chem. Rev.* **2022**, *451*, 214260.
- [7] X. Liu, Y. Cao, J. Sun, *Adv. Energy Mater.* **2022**, *12*, 2202532.
- [8] J. Xiao, X. Li, K. Tang, D. Wang, M. Long, H. Gao, W. Chen, C. Liu, H. Liu, G. Wang, *Mater. Chem. Front.* **2021**, *5*, 3735.
- [9] X. Guo, H. Gao, S. Wang, G. Yang, X. Zhang, J. Zhang, H. Liu, G. Wang, *Nano Lett.* **2022**, *22*, 1225.
- [10] H. Gao, J. Li, F. Zhang, C. Li, J. Xiao, X. Nie, G. Zhang, Y. Xiao, D. Zhang, X. Guo, Y. Wang, Y. M. Kang, G. Wang, H. Liu, *Adv. Energy Mater.* **2024**, 2304529.
- [11] J. Xiao, Y. Xiao, J. Li, C. Gong, X. Nie, H. Gao, B. Sun, H. Liu, G. Wang, *SmartMat* **2023**, *4*, e1211.
- [12] J. Qian, C. Wu, Y. Cao, Z. Ma, Y. Huang, X. Ai, H. Yang, *Adv. Energy Mater.* **2018**, *8*, 1702619.
- [13] J. Peng, W. Zhang, Q. Liu, J. Wang, S. Chou, H. Liu, S. Dou, *Adv. Mater.* **2022**, *34*, 2108384.
- [14] K. Itaya, N. Shoji, I. Uchida, *J. Am. Chem. Soc.* **1984**, *106*, 3423.
- [15] W. Yiting, Z. Jianzhong, Z. Rongjin, Z. Ziqiang, L. Zongsheng, C. Zongyou, *Meas. Sci. Technol.* **2003**, *14*, 831.
- [16] S. Sindhu, K. Narasimha Rao, S. Ahuja, A. Kumar, E. S. R. Gopal, *Mater. Sci. Eng. B* **2006**, *132*, 129.
- [17] R. Jurgons, C. Seliger, A. Hilpert, L. Trahms, S. Odenbach, C. Alexiou, *J. Phys. Condens Matter* **2006**, *18*, S2893.
- [18] L. Wang, J. Song, R. Qiao, L. A. Wray, M. A. Hossain, Y.-D. Chuang, W. Yang, Y. Lu, D. Evans, J.-J. Lee, S. Vail, X. Zhao, M. Nishijima, S. Kakimoto, J. B. Goodenough, *J. Am. Chem. Soc.* **2015**, *137*, 2548.
- [19] R. Chen, Y. Huang, M. Xie, Z. Wang, Y. Ye, L. Li, F. Wu, *ACS Appl. Mater. Interfaces* **2016**, *8*, 31669.
- [20] M. Morant-Giner, R. Sanchis-Gual, J. Romero, A. Alberola, L. García-Cruz, S. Agouram, M. Galbiati, N. M. Padial, J. C. Waerenborgh, C. Martí-Gastaldo, S. Tatay, A. Forment-Aliaga, E. Coronado, *Adv. Funct. Mater.* **2018**, *28*, 1706125.
- [21] Y. Huang, M. Xie, Z. Wang, Y. Jiang, Y. Yao, S. Li, Z. Li, L. Li, F. Wu, R. Chen, *Small* **2018**, *14*, 1801246.
- [22] P. Hu, W. Peng, B. Wang, D. Xiao, U. Ahuja, J. Réthoré, K. E. Aifantis, *ACS Energy Lett.* **2020**, *5*, 100.
- [23] Y. Ma, Y. Ma, S. L. Dreyer, Q. Wang, K. Wang, D. Goonetilleke, A. Omar, D. Mikhailova, H. Hahn, B. Breitung, T. Brezesinski, *Adv. Mater.* **2021**, *33*, 2101342.
- [24] S. He, J. Zhao, X. Rong, C. Xu, Q. Zhang, X. Shen, X. Qi, Y. Li, X. Li, Y. Niu, X. Li, S. Han, L. Gu, H. Liu, Y.-S. Hu, *Chem. Eng. J.* **2022**, *428*, 131083.
- [25] M. Wan, R. Zeng, J. Meng, Z. Cheng, W. Chen, J. Peng, W. Zhang, Y. Huang, *Nanomicro Lett* **2022**, *14*, 9.
- [26] R. Wei, X. Zhai, H. R. Tinker, P. He, C. A. F. Nason, Y. Han, V. Celorrio, G. Sankar, M. Zhou, Y. Xu, *Adv. Funct. Mater.* **2023**, *33*, 2308227.
- [27] Y. Wang, N. Jiang, C. Yang, J. Liu, S. Sun, X. Wang, J. Yang, Y. Liu, *J. Mater. Chem. A* **2024**, *12*, 5170.
- [28] H. Yi, R. Qin, S. Ding, Y. Wang, S. Li, Q. Zhao, F. Pan, *Adv. Funct. Mater.* **2021**, *31*, 2006970.
- [29] Y. Yue, A. J. Binder, B. Guo, Z. Zhang, Z. A. Qiao, C. Tian, S. Dai, *Angew. Chem., Int. Ed.* **2014**, *53*, 3134.
- [30] X. Song, S. Song, D. Wang, H. Zhang, *Small Methods* **2021**, *5*, 2001000.
- [31] L. Ma, H. Cui, S. Chen, X. Li, B. Dong, C. Zhi, *Nano Energy* **2021**, *81*, 105632.
- [32] L. Ge, Y. Song, P. Niu, B. Li, L. Zhou, W. Feng, C. Ma, X. Li, D. Kong, Z. Yan, Q. Xue, Y. Cui, W. Xing, *ACS Nano* **2024**, *18*, 3542.
- [33] J. Sun, H. Ye, J. A. S. Oh, A. Plewa, Y. Sun, T. Wu, Q. Sun, K. Zeng, L. Lu, *Energy Storage Mater.* **2021**, *43*, 182.
- [34] L. Ma, S. Chen, C. Long, X. Li, Y. Zhao, Z. Liu, Z. Huang, B. Dong, J. A. Zapien, C. Zhi, *Adv. Energy Mater.* **2019**, *9*, 1902446.
- [35] Z. Wang, Y. Huang, D. Chu, C. Li, Y. Zhang, F. Wu, L. Li, M. Xie, J. Huang, R. Chen, *ACS Appl. Mater. Interfaces* **2021**, *13*, 38202.
- [36] L.-P. Wang, P.-F. Wang, T.-S. Wang, Y.-X. Yin, Y.-G. Guo, C.-R. Wang, *J. Power Sources* **2017**, *355*, 18.
- [37] A. Zhou, W. Cheng, W. Wang, Q. Zhao, J. Xie, W. Zhang, H. Gao, L. Xue, J. Li, *Adv. Energy Mater.* **2021**, *11*, 2000943.
- [38] X. Wu, M. Sun, S. Guo, J. Qian, Y. Liu, Y. Cao, X. Ai, H. Yang, *Chem-NanoMat* **2015**, *1*, 188.
- [39] J. Song, L. Wang, Y. Lu, J. Liu, B. Guo, P. Xiao, J.-J. Lee, X.-Q. Yang, G. Henkelman, J. B. Goodenough, *J. Am. Chem. Soc.* **2015**, *137*, 2658.
- [40] M. Qin, W. Ren, J. Meng, X. Wang, X. Yao, Y. Ke, Q. Li, L. Mai, *ACS Sustainable Chem. Eng.* **2019**, *7*, 11564.
- [41] M. Oliver-Tolentino, G. Ramos-Sánchez, G. Guzmán, M. Avila, I. González, E. Reguera, *Solid State Ion* **2017**, *312*, 67.
- [42] C. Islas-Vargas, A. Guevara-García, M. Oliver-Tolentino, G. Ramos-Sánchez, I. González, M. Galván, *J. Electrochem. Soc.* **2019**, *166*, A5139.
- [43] F. Gebert, D. L. Cortie, J. C. Bower, W. Wang, Z. Yan, S. X. Dou, S. L. Chou, *Angew. Chem., Int. Ed.* **2021**, *60*, 18519.
- [44] M. Zhang, R. Liang, T. Or, Y.-P. Deng, A. Yu, Z. Chen, *Small Struct.* **2021**, *2*, 2000064.
- [45] Y. Shang, X. Li, J. Song, S. Huang, Z. Yang, Z. J. Xu, H. Y. Yang, *Chem* **2020**, *6*, 1804.
- [46] L. Shen, Y. Jiang, Y. Liu, J. Ma, T. Sun, N. Zhu, *Chem. Eng. J.* **2020**, *388*, 124228.
- [47] W. Ren, X. Chen, C. Zhao, *Adv. Energy Mater.* **2018**, *8*, 1801413.
- [48] G. Ni, B. Han, Q. Li, Z. Ji, B. Huang, C. Zhou, *ChemElectroChem* **2016**, *3*, 798.

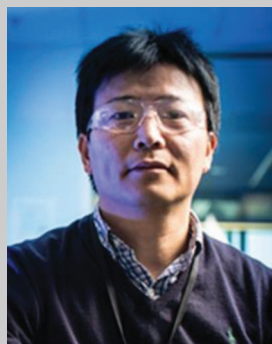
- [49] M. Shao, B. Wang, M. Liu, C. Wu, F.-S. Ke, X. Ai, H. Yang, J. Qian, *ACS Appl. Energy Mater.* **2019**, *2*, 5809.
- [50] M. Jiang, Z. Hou, L. Ren, Y. Zhang, J.-G. Wang, *Energy Storage Mater.* **2022**, *50*, 618.
- [51] J. Wu, J. Song, K. Dai, Z. Zhuo, L. A. Wray, G. Liu, Z.-x. Shen, R. Zeng, Y. Lu, W. Yang, *J. Am. Chem. Soc.* **2017**, *139*, 18358.
- [52] C. D. Wessells, S. V. Peddada, R. A. Huggins, Y. Cui, *Nano Lett.* **2011**, *11*, 5421.
- [53] C. D. Wessells, S. V. Peddada, M. T. McDowell, R. A. Huggins, Y. Cui, *J. Electrochem. Soc.* **2012**, *159*, A98.
- [54] J. Peng, M. Ou, H. Yi, X. Sun, Y. Zhang, B. Zhang, Y. Ding, F. Wang, S. Gu, C. A. López, W. Zhang, Y. Liu, J. Fang, P. Wei, Y. Li, L. Miao, J. Jiang, C. Fang, Q. Li, M. T. Fernández-Díaz, J. A. Alonso, S. Chou, J. Han, *Energy Environ. Sci.* **2021**, *14*, 3130.
- [55] W. Ren, M. Qin, Z. Zhu, M. Yan, Q. Li, L. Zhang, D. Liu, L. Mai, *Nano Lett.* **2017**, *17*, 4713.
- [56] Y. Xu, J. Wan, L. Huang, M. Ou, C. Fan, P. Wei, J. Peng, Y. Liu, Y. Qiu, X. Sun, C. Fang, Q. Li, J. Han, Y. Huang, J. A. Alonso, Y. Zhao, *Adv. Energy Mater.* **2019**, *9*, 1803158.
- [57] Y. Lu, L. Wang, J. Cheng, J. B. Goodenough, *ChemComm* **2012**, *48*, 6544.
- [58] Y. You, X.-L. Wu, Y.-X. Yin, Y.-G. Guo, *Energy Environ. Sci.* **2014**, *7*, 1643.
- [59] T. Matsuda, M. Takachi, Y. Moritomo, *ChemComm* **2013**, *49*, 2750.
- [60] J. Peng, Y. Gao, H. Zhang, Z. Liu, W. Zhang, L. Li, Y. Qiao, W. Yang, J. Wang, S. Dou, S. Chou, *Angew. Chem., Int. Ed.* **2022**, *61*, 202205867.
- [61] Y. Tang, W. Li, P. Feng, M. Zhou, K. Wang, Y. Wang, K. Zaghbi, K. Jiang, *Adv. Funct. Mater.* **2020**, *30*, 1908754.
- [62] X. Wu, W. Deng, J. Qian, Y. Cao, X. Ai, H. Yang, *J. Mater. Chem. A* **2013**, *1*, 10130.
- [63] Y. P. Wang, B. P. Hou, X. R. Cao, S. Q. Wu, Z. Z. Zhu, *J. Electrochem. Soc.* **2022**, *169*, 010525.
- [64] M. Chen, Y. Zhang, G. Xing, Y. Tang, *Front Chem* **2020**, *8*, 152.
- [65] J. Peng, J. Wang, H. Yi, W. Hu, Y. Yu, J. Yin, Y. Shen, Y. Liu, J. Luo, Y. Xu, P. Wei, Y. Li, Y. Jin, Y. Ding, L. Miao, J. Jiang, J. Han, Y. Huang, *Adv. Energy Mater.* **2018**, *8*, 1702856.
- [66] J. Nordstrand, E. Toledo-Carrillo, S. Vafakhah, L. Guo, H. Y. Yang, L. Kloo, J. Dutta, *ACS Appl. Mater. Interfaces* **2021**, *14*, 1102.
- [67] H. Lee, Y.-I. Kim, J.-K. Park, J. W. Choi, *ChemComm* **2012**, *48*, 8416.
- [68] S. Jiao, J. Tuo, H. Xie, Z. Cai, S. Wang, J. Zhu, *Mater. Res. Bull.* **2017**, *86*, 194.
- [69] L. Wang, Y. Lu, J. Liu, M. Xu, J. Cheng, D. Zhang, J. B. Goodenough, *Angew. Chem., Int. Ed.* **2013**, *52*, 1964.
- [70] K. Hurlbutt, S. Wheeler, I. Capone, M. Pasta, *Joule* **2018**, *2*, 1950.
- [71] M. Chen, Q. Liu, S. W. Wang, E. Wang, X. Guo, S. L. Chou, *Adv. Energy Mater.* **2019**, *9*, 1803609.
- [72] A. Paoletta, C. Faure, V. Timoshevskii, S. Marras, G. Bertoni, A. Guerfi, A. Vijn, M. Armand, K. Zaghbi, *J. Mater. Chem. A* **2017**, *5*, 18919.
- [73] Q.-L. Zhu, P. Pachfule, P. Strubel, Z. Li, R. Zou, Z. Liu, S. Kaskel, Q. Xu, *Energy Storage Mater.* **2018**, *13*, 72.
- [74] X. Tang, H. Liu, D. Su, P. H. L. Notten, G. Wang, *Nano Res.* **2018**, *11*, 3979.
- [75] Y. You, X. Yu, Y. Yin, K.-W. Nam, Y.-G. Guo, *Nano Res.* **2015**, *8*, 117.
- [76] W. Wang, Y. Gang, J. Peng, Z. Hu, Z. Yan, W. Lai, Y. Zhu, D. Appadoo, M. Ye, Y. Cao, Q. F. Gu, H. K. Liu, S. X. Dou, S. L. Chou, *Adv. Funct. Mater.* **2022**, *32*, 2111727.
- [77] B. Wang, S. Liu, W. Sun, Y. Tang, H. Pan, M. Yan, Y. Jiang, *ChemSusChem* **2019**, *12*, 2415.
- [78] D. Yang, J. Xu, X.-Z. Liao, Y.-S. He, H. Liu, Z.-F. Ma, *Chem. Commun.* **2014**, *50*, 13377.
- [79] W.-J. Li, S.-L. Chou, J.-Z. Wang, Y.-M. Kang, J.-L. Wang, Y. Liu, Q.-F. Gu, H.-K. Liu, S.-X. Dou, *Chem. Mater.* **2015**, *27*, 1997.
- [80] R. Chen, Y. Huang, M. Xie, Q. Zhang, X. Zhang, L. Li, F. Wu, *ACS Appl. Mater. Interfaces* **2016**, *8*, 16078.
- [81] M. Hu, S. Furukawa, R. Ohtani, H. Sukegawa, Y. Nemoto, J. Reboul, S. Kitagawa, Y. Yamauchi, *Angew. Chem., Int. Ed.* **2012**, *51*, 984.
- [82] Y. Li, Q. Dang, W. Chen, L. Tang, M. Hu, *J. Inorg. Organomet. P* **2021**, *31*, 1877.
- [83] W. Tang, Y. Xie, F. Peng, Y. Yang, F. Feng, X.-Z. Liao, Y.-S. He, Z.-F. Ma, Z. Chen, Y. Ren, *J. Electrochem. Soc.* **2018**, *165*, A3910.
- [84] Z. Liang, F. Tian, G. Yang, C. Wang, *Nat. Commun.* **2023**, *14*, 3591.
- [85] K. Hurlbutt, F. Giustino, G. Volonakis, M. Pasta, *Chem. Mater.* **2022**, *34*, 4336.
- [86] A. Rudola, K. Du, P. Balaya, *J. Electrochem. Soc.* **2017**, *164*, A1098.
- [87] W. R. Brant, R. Mogensen, S. Colbin, D. O. Ojwang, S. Schmid, L. Häggström, T. Ericsson, A. Jaworski, A. J. Pell, R. Younesi, *Chem. Mater.* **2019**, *31*, 7203.
- [88] W. Wang, Y. Gang, Z. Hu, Z. Yan, W. Li, Y. Li, Q.-F. Gu, Z. Wang, S.-L. Chou, H.-K. Liu, S.-X. Dou, *Nat. Commun.* **2020**, *11*, 980.
- [89] J. Peng, J. Huang, Y. Gao, Y. Qiao, H. Dong, Y. Liu, L. Li, J. Wang, S. Dou, S. Chou, *Small* **2023**, *19*, 2300435.
- [90] Y. Xu, M. Ou, Y. Liu, J. Xu, X. Sun, C. Fang, Q. Li, J. Han, Y. Huang, *Nano Energy* **2020**, *67*, 104250.
- [91] J. Peng, C. Li, J. Yin, J. Wang, Y. Yu, Y. Shen, J. Fang, A. Chen, Y. Xu, R. Rehman, C. Fang, L. Miao, R. Jiang, Q. Li, J. Han, Y. Huang, *ACS Appl. Energy Mater.* **2019**, *2*, 187.
- [92] H. L. B. Boström, I. E. Collings, D. Daisenberger, C. J. Ridley, N. P. Funnell, A. B. Cairns, *J. Am. Chem. Soc.* **2021**, *143*, 3544.
- [93] J. Sun, H. Ye, J. A. S. Oh, Y. Sun, A. Plewa, Y. Wang, T. Wu, K. Zeng, L. Lu, *Nano Res.* **2022**, *15*, 2123.
- [94] C. Xu, Y. Ma, J. Zhao, P. Zhang, Z. Chen, C. Yang, H. Liu, Y. S. Hu, *Angew. Chem., Int. Ed.* **2023**, *62*, 202217761.
- [95] Y. Tang, L. Wang, J. Hu, M. Chen, M. Zhou, K. Wang, K. Jiang, *Adv. Energy Mater.* **2024**, *14*, 2303015.
- [96] M. Takachi, T. Matsuda, Y. Moritomo, *Appl. Phys. Express* **2013**, *6*, 025802.
- [97] J. Liu, J. Liu, M. Tang, J. Fu, X. Kuang, J. Ma, *Adv. Funct. Mater.* **2024**, *2314167*.
- [98] X. Liu, H. Gong, C. Han, Y. Cao, Y. Li, J. Sun, *Energy Storage Mater.* **2023**, *57*, 118.
- [99] X. Zhao, Z. Xing, C. Huang, *J. Mater. Chem. A* **2023**, *11*, 22835.
- [100] W. Jiang, T. Wang, H. Chen, X. Suo, J. Liang, W. Zhu, H. Li, S. Dai, *Nano Energy* **2021**, *79*, 105464.
- [101] Y. Ma, Y. Hu, Y. Pramudya, T. Diemant, Q. Wang, D. Goonetilleke, Y. Tang, B. Zhou, H. Hahn, W. Wenzel, M. Fichtner, Y. Ma, B. Breitung, T. Brezesinski, *Adv. Funct. Mater.* **2022**, *32*, 2202372.
- [102] J. Peng, B. Zhang, W. Hua, Y. Liang, W. Zhang, Y. Du, G. Peleckis, S. Indris, Q. Gu, Z. Cheng, J. Wang, H. Liu, S. Dou, S. Chou, *Angew. Chem., Int. Ed.* **2023**, *62*, 202215865.
- [103] V. T. Nguyen, F. N. I. Sari, B. W. Saputro, J.-M. Ting, *J. Mater. Chem. A* **2023**, *11*, 19483.
- [104] Y. Huang, X. Zhang, L. Ji, L. Wang, B. B. Xu, M. W. Shahzad, Y. Tang, Y. Zhu, M. Yan, G. Sun, Y. Jiang, *Energy Storage Mater.* **2023**, *58*, 1.
- [105] J. Dai, S. Tan, L. Wang, F. Ling, F. Duan, M. Ma, Y. Shao, X. Rui, Y. Yao, E. Hu, X. Wu, C. Li, Y. Yu, *ACS Nano* **2023**, *17*, 20949.
- [106] Y. He, S. L. Dreyer, Y. Y. Ting, Y. Ma, Y. Hu, D. Goonetilleke, Y. Tang, T. Diemant, B. Zhou, P. M. Kowalski, M. Fichtner, H. Hahn, J. Aghassi-Hagmann, T. Brezesinski, B. Breitung, Y. Ma, *Angew. Chem., Int. Ed.* **2023**, *63*, 202315371.
- [107] X. H. Liu, J. Peng, W. H. Lai, Y. Gao, H. Zhang, L. Li, Y. Qiao, S. L. Chou, *Adv. Funct. Mater.* **2022**, *32*, 2108616.



Yang Xiao obtained his bachelor's degree in Chemical Engineering and Technology at Hefei University of Technology in 2021. He is pursuing his master's degree at Shanghai University. His research interest mainly focuses on Prussian blue cathode materials for sodium-ion batteries.



Hong Gao is presently serving as an Associate Professor at Shanghai University. She completed her Ph.D. in Material Science at the University of Wollongong, Australia, in 2018. Following her doctoral studies, she assumed the role of faculty postdoctoral fellow at Shanghai University before transitioning to the University of Technology Sydney as a Research Associate. Her research pursuits center on the synthesis and applications of advanced functional materials tailored for energy storage and conversion applications.



Jun Chen is currently appointed as Deputy Director of Intelligent Polymer Research Institute (IPRI), University of Wollongong (UOW). His research interests include: Electroactive Materials, Electro-/Bio- Interfaces, Nano/Micro- Materials, 2D/3D Printing and Wearable Electronic Devices. In 2021, Prof. Chen has been admitted as a *Fellow of The Royal Society of Chemistry* (FRSC). Professor Chen has been identified as *Highly Cited Researchers* in Cross Field (5 times) since 2018.



Hao Liu is a Full Professor and ARC Future Fellow at University of Technology Sydney (UTS). He obtained his PhD degree from the University of Wollongong in 2011. He worked as a research associate at the University of Queensland and moved to the University of Technology Sydney as a Chancellor's postdoctoral research fellow. He is interested in the synthesis of nanostructured materials and their applications in the fields of lithium-ion batteries, sodium-ion batteries, lithium-sulfur batteries, lithium-oxygen batteries, supercapacitors, and electrocatalysts.